Water-air flow in straight pipes and across 90 degrees sharp-angled mitre elbows

Wameedh T.M. Al-Tameemi[a,*], Pierre Ricco[b]

[a]*Reconstruction and Project Directorate, Ministry of Higher Education and Scientific Research, Baghdad, Iraq*
[b]*Department of Mechanical Engineering, The University of Sheffield, S1 3JD, UK*

Abstract

Accepted for publication in Int. J. Multiph. Flow.

Water-air flow in horizontal and vertical straight pipes and through 90° sharp-angled mitre elbows is investigated by visualizing the flow patterns by means of a high-precision camera and by measuring the pressure drop. The flow is studied in pipes with three diameters for about six hundred conditions of water-air flows, characterized by superficial velocities in the ranges of j_L^*=0.3-1m/s for water and j_G^*=0.15-34m/s for air. The portion of the pipe upstream of the elbow is always positioned horizontally, while the portion of the pipe downstream of the sharp bend is oriented horizontally or vertically with the flow moving upward. Plug, slug, slug-annular, and annular flows are visualized in horizontal straight pipes, while slug, churn, and annular regimes are recorded in vertical straight pipes downstream of the sharp bend. These patterns are well predicted by the Mandhane map (J. Mandhane, G. Gregory, K. Aziz, A flow pattern map for gas-liquid flow in horizontal pipes, Int. J. Multiph. Flow 1 (4) (1974) 537-553) for horizontally oriented straight pipes and by the Hewitt-Roberts map (G. Hewitt, D. Roberts, Studies of two-phase flow patterns by simultaneous 292 X-ray and flash photography, Tech. Rep., Atomic Energy Research Establishment, Harwell (England) (1969)) for vertically oriented straight pipes. The changes of the flow patterns as the fluids pass through the mitre elbows are discussed. A multiple membrane flow structure is observed in the vertical upward flow at much higher Reynolds numbers based on the water superficial velocity than in the vertical downward case previously reported in the literature. A dimensional analysis is employed to obtain the non-dimensional parameters that describe the flows through the straight pipes and across the elbows. It is proved that a rigorous way to present the flow regimes and the pressure-drop coefficients of the water-air flow for a given geometry is the space of the Reynolds numbers based on the superficial velocities of air and water for fixed Froude number because the flow is incompressible and isothermal. By expressing the maps in scaled form, the prediction of the flow patterns along the straight portions of the pipe improves. The flow patterns through the elbows are expressed in terms of rescaled Mandhane maps, which, for the first time, simultaneously represent the flow patterns both upstream and downstream of the elbows. New pattern-based empirical correlations are obtained for the scaled pressure drops for the water-air flows through the horizontal and vertical pipes and through the elbows. The correlations are based on the flow patterns and do not rely on widely used prediction models, thereby predicting the pressure drop more accurately than the models presently available in the literature.

Keywords: `Two-phase flow`, `flow patterns`, `pressure drop`, `sharp-angled mitre elbow`

1. Introduction

Two-phase flow through pipes and ducts is common in many industrial applications, such as chemical, nuclear, gas, and oil systems. The prediction of pressure drops in these systems in the presence of fittings, such as elbows and valves, represents an essential issue to designers because the pressure drop is affected by many factors, such as the geometry, the properties of the fluids, and the flow patterns. The prediction of the flow patterns through pipe fittings is particularly important for the design of industrial piping systems because the flow regimes regulate relevant flow properties, like the pressure drop and the heat transfer [1].

Many researchers have proposed pressure-drop prediction models for two-phase flow in straight pipes [2, 3, 4, 5, 6], while a very limited number of models have been proposed for the pressure drop across 90° round elbows [7, 8, 9, 10] and 180° bends [11, 12]. Most of these models expressed the two-phase pressure drop in terms of a

---

*Wameedh T.M. Al-Tameemi

Email address: `wameedh.altameemi@gmail.com` (Wameedh T.M. Al-Tameemi)

two-phase multiplier ϕ as:

$$\Delta p^* = \phi \, \Delta p_k^*, \tag{1}$$

where Δp_k^* is the single-phase pressure drop in straight pipes and the subscript k denotes the fluid phase, i.e., $k=L$ for the liquid phase and $k=G$ for the gas phase.

Many maps have been proposed for the prediction of the adiabatic water-air flow patterns in straight pipes in the horizontal configuration, such as the Mandhane map [13], and in the vertical configuration, such as the Hewitt-Roberts map [14]. Ghajar and Tang [15] proposed maps for both cases. Although these maps are based on dimensional values, they have the ability to identify the flow patterns for a wide range of flow conditions within acceptable error. Nevertheless, there are many two-phase phenomena occurring in flows through pipe fittings, like valves and bends, that are difficult to represent in a single flow pattern map. Many research efforts have focused on the effect of common pipe fittings, such as 90° round elbows and 180° bends, on the two-phase flow patterns and have reported phenomena that are usually observed in both horizontal and vertical orientations. Chen *et al.* [16] and Wang *et al.* [11, 17, 18] showed that the flow regime changes suddenly from stratified to annular through horizontal and vertical 180° bends with low curvature ratios because the centrifugal forces overcome the effect of gravity. The phenomena of reverse flow and slug division and merging in the vertical configuration were reported by Wang *et al.* [18] for 180° bends and Hsu *et al.* [19] for 90° round elbows. Milan *et al.* [20] recently discovered the membrane flow, a new two-phase flow structure in vertical downward water-air flows through straight pipes that may develop downstream of phase-mixers as a result of coalescence of bubbles and liquid-slug shrinkage.

It is also crucial to calculate two flow perturbation lengths. One length is the distance downstream of the elbow that is required by the flow to recover the constant pressure gradient and the patterns observed well upstream of the bend. The other length is the perturbation distance upstream of the elbow at which the flow starts to be influenced by the presence of the elbow. The downstream recovery distance for different bends and for different working fluids was found to vary between $10D^*$ and $60D^*$, while the upstream perturbation length was estimated to be shorter, ranging between $5D^*$ and $40D^*$ [21, 22, 23, 24]. For 90° round elbows in particular, the perturbation lengths were found to be smaller than $44D^*$ downstream of the bend in horizontal bubbly flow by Kim *et al.* [25], while Yadav *et al.* [26, 27] showed they are smaller than $16D^*$ upstream and $33D^*$ downstream of vertical elbows.

Although the two-phase pressure drop is highly influenced by the flow patterns [9, 1], pattern-based pressure drop prediction models are very limited in the literature [28, 29]. Furthermore, the models for flows across pipe fittings predict the frictional pressure drop without considering the effect of the flow separation, which is the main cause of the losses in sharp-angled mitre elbows. Despite a few investigations on single-phase flow across 90° sharp-angled elbows for laminar [30, 31, 32] and turbulent flows [33, 34, 35], to the best of our knowledge, no study in the literature has examined the pressure drop and flow patterns of the two-phase flow in this type of fittings. Mitre bends are widely used in many industrial applications, especially those requiring large-diameter piping in the chemical, nuclear, and oil industries [36]. Designers of these systems employ the mitre bends mainly because of space and economic limitations [36].

In this work, we are therefore motivated to investigate the patterns and the pressure drops of water-air flows upstream, through, and downstream of 90° sharp-angled mitre elbows in horizontal and vertical orientations. The flows are studied in pipes and elbows positioned horizontally and vertically with the flow moving upward. Important aims are to assess how the flow patterns change character as the fluids pass through the sharp elbows and to represent these changes by use of the Mandhane map [13]. By exploiting a simple dimensional analysis, we propose a novel visual representation that allows the simultaneous identification of the flow patterns upstream and downstream of the sharp bends in a single non-dimensional Mandhane map for each elbow orientation. Other aims are to obtain pattern-based pressure drop empirical correlations for the flows in the straight pipes and across the mitre elbows and to find the flow recovery lengths downstream of the bend and the perturbation length upstream of the bend.

This research work continues our research investigation on flows across mitre elbows, i.e., the study of the pressure drop for single-phase flow [35] and the flow visualization and pressure-loss measurements in two-phase flow conditions [37]. The present paper differs from the latter because in [37] we only used a pipe with one diameter in the horizontal configuration and employed the Lockhart-Martinelli model to scale the pressure drop, while in the present work pipes with three different diameters were used for both horizontal and vertical orientations and novel correlations for the scaled pressure drops in all the configurations were obtained.

The experimental facility is described in §2.1, the experimental procedures are discussed in §2.2, while the uncertainty analysis is given in §2.3. The flow visualization of the water-air patterns and their representations in the flow-pattern maps are presented in §3.1 and the study of the pressure drop along the straight portions of the pipes and across the sharp bends is reported in §3.2. Conclusions are found in §4.
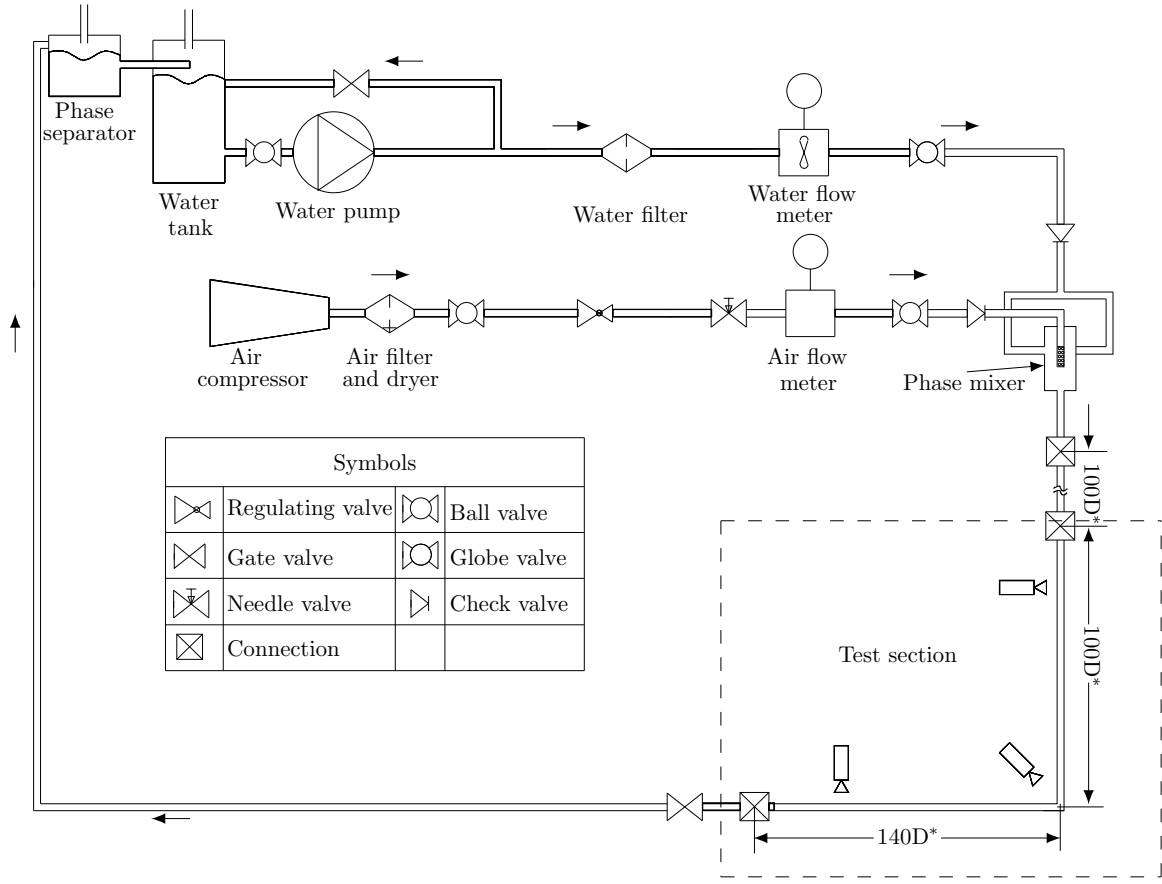
2

Figure 1: Schematic diagram of the experimental facility.

2. Experimental apparatus and procedures

2.1. Experimental apparatus

The facility was designed and built for this research work in the Department of Mechanical Engineering at The University of Sheffield. The rig is shown schematically in Fig. 1 and described in further detail in two papers of ours [35, 37]. It was composed of air and water lines, a mixer of the two fluids, and the test section equipped with the 90° sharp-angled mitre elbow. The part of the pipe downstream of the bend was positioned horizontally or vertically with the flow moving upward, whereas the part of the pipe upstream of the bend was always oriented horizontally.

A variable speed pump was used to supply the test sections with water at different flow rates at the needed operating pressure (up to 6bar). Two turbine type water flow meters were utilized to measure the flow rates. The flow meter Omega-FTB-101 measured flow rates in the range 1.3-13.2 l/min and the flow meter Omega-FTB-104 measured flow rates in the range 6.6-60 l/min. The flow meters were calibrated by the manufacturer with a ±0.5% of the measured flow-rate uncertainty. The air was supplied to the facility from an outlet air compressor at a pressure of 7 bar. A filter dryer and a pressure regulator were used to regulate the air flow rates manually. The flow meter Omega FMA-1612A-v2 was used to measure the air flow rate in the range 2.5-500 standard l/min and it was calibrated by the manufacturer with a ±0.8% accuracy of the reading ±0.2% of the full scale uncertainty.

A phase mixer was designed and assembled to generate the water-air mixture. Air entered the mixer parallel to its axis through a section of porous media characterized by holes with 0.1mm diameter. Two jets of water entered the mixer from opposite sides and perpendicularly to the axis of the mixer. The water-air mixture left the mixer towards the test section from the opposite side of the air entrance. Three different test sections were assembled by employing acrylic pipes with 11, 16, and 21mm diameters and 2mm wall thickness. Ten measurement stations were located along each test section to measure the pressure drop. The sharp-angled elbows were assembled by cutting two pieces of pipe at 45° and by joining them by using a special acrylic welding solution.

3

Two different pressure transducers, Omega PX409-2.5DWU10V and Omega PX409-10WDWUI, were used to measure the pressure drop along the test sections and across the elbows. They operated in the ranges 0-17.2 kPa and 0-2.5 kPa, respectively. The transducers were calibrated by the manufacturer with a 0.8% accuracy of the full scale best-straight-fit-line accuracy. The pressure signals were recorded by a National Instrument data acquisition system with 16-bit resolution, which consisted of an NI-USB-6002 card for voltage signal and an NI-9203-analogue-channel with an NI-CDAQ-9171-USB-Chasis for current signals.

A high-speed high-resolution camera Phantum V-210 was used for video capturing. The visual observation method was chosen to distinguish the flow patterns along the straight pipes and through the sharp-angled elbows. This method is routinely employed to characterize the flow patterns and other flow phenomena [38, 39, 40]. Two mirrors were fixed at 45° downstream and upstream of the horizontal sharp bend to capture the side and top views of the flow patterns, as illustrated in Fig. 2.
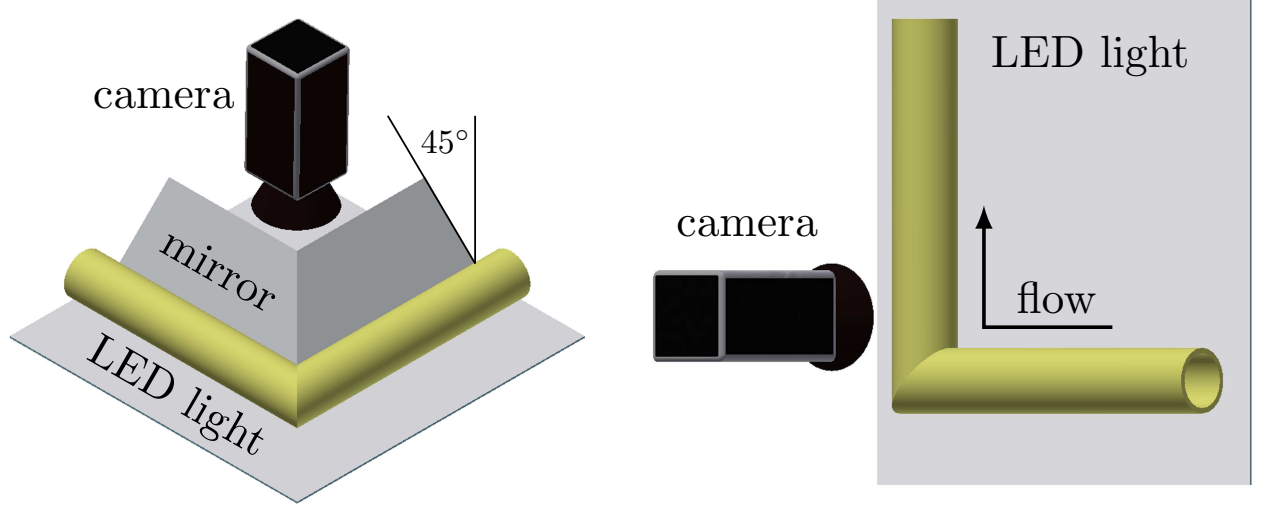

Figure 2: Schematic diagram of the camera in the horizontal (left) and the vertical (right) orientations.

2.2. Experimental procedures

Table 1: Flow parameters in the horizontal configuration.

D^*(mm)	j_L^* (m/s)	j_G^* (m/s)	$\mathcal{R}e_L$	$\mathcal{R}e_G$
11	0.51 - 0.76	0.51 - 33.82	5173 - 10346	293 - 19559
16	0.55 - 0.79	0.26 - 30.59	7945 - 11367	208 - 24956
21	0.297 - 0.68	0.15 - 24.75	5598 - 12782	158 - 26456

Table 2: Flow parameters in the vertical configuration.

D^*(mm)	j_L^* (m/s)	j_G^* (m/s)	$\mathcal{R}e_L$	$\mathcal{R}e_G$
11	0.68 - 1.02	0.51 - 30.44	6897 - 10346	293 - 17603
16	0.34 - 0.68	0.26 - 33.99	4889 - 9778	208 - 27729
21	0.279 - 0.50	0.15 - 24.75	5598 - 9330	158 - 26456

Several superficial velocities for air and water, $j_k^*=\dot{V}_k^*/\mathcal{A}^*$, were used, where $\dot{V}_k^*$ is the volumetric flow rate of air and water, the subscript $k=G$ denotes air and the subscript $k=L$ indicates water, and $\mathcal{A}^*$ is the cross-sectional area of the pipe. In the horizontal configuration, five j_L^* were used in the pipe with D^*=21mm, while three j_L^* were used when D^*=11 and 16mm. About 15, 20, and 30 j_G^* in the ranges listed in Table 1 were employed for each j_L^* in the pipes with D^*=11, 16, and 21mm, respectively. In the vertical orientation, five j_L^* were used for each test section, while 12, 20, and 30 j_G^* were used for each j_L^* in the pipes with D^*=11, 16, and 21mm, respectively. The vertical flow conditions are listed in Table 2. Appendix A describes the methodology to calculate the frictional pressure drop along the vertical and horizontal straight pipes and Appendix B presents the procedure for the computation of the pressure drop due to the sharp elbow.

2.3. Uncertainty analysis

The uncertainties in the measured values included the uncertainty of the pipe diameter D^*, the distance between two adjacent measurement stations Δl^*, the surface roughness of the pipes, the elbow angles, and the physical properties of the fluids. Each pipe diameter was measured carefully by a micrometer at five different locations with a ± 0.1mm maximum error, while the surface roughness of the pipe was measured by a Dektal 150 surface profiler with a $\pm 2\%$ uncertainty. The distances Δl^* were measured with a ± 1mm maximum error and the angle of the elbows was measured by an accurate protractor with a $\pm 0.5°$ uncertainty. The uncertainty of the fluid properties was computed by using the NIST Refprop database [41]. The square root of the sum of the sequence method was used to obtain the total uncertainty of a measured quantity $f = f(x_0, .., x_N)$, as follows [42]:

$$\delta f = \sqrt{\sum_{n=0}^{N} \left(\frac{\partial f}{\partial x_n} \, \delta x_n \right)^2},\tag{2}$$

where δx_n is the experimental error associated with the variable x_n and N is the number of data points. A large number of experiments were independently repeated to guarantee the robustness and high quality of the measurements. The average error of all the repeated experimental data was about 2.3%. The total uncertainties for each flow condition are shown as error bars in the figures presenting the scaled pressure drops in §3.

The accuracy of the correlations obtained in §3.2 was determined by the mean absolute percentage error,

$$\mathcal{E}(\%) = \frac{100\%}{N} \sum_{i=1}^{N} \frac{|f_{i,pred} - f_{i,exp}|}{f_{i,exp}},\tag{3}$$

where f in (3) indicates the pressure-drop coefficients $\mathcal{C}_L$ or $\mathcal{K}_L$ defined in §3.2, the subscripts "pred" and "exp" denote the values predicted via the correlations and the values measured experimentally, respectively.

3. Results

3.1. Analysis of flow visualizations

3.1.1. Flow patterns in straight pipes

Four flow patterns were observed in the horizontal configuration for 275 flow conditions for air and water superficial velocities in the ranges listed in Table 1: plug, slug, slug-annular, and annular flows. Fig. 3 presents instantaneous snapshots of these patterns in the flow upstream of the bend along the horizontal 21-mm-diameter pipe for j_L^*=0.495m/s and different j_G^*. Different flow visualizations of water-air patterns in the 21-mm-diameter pipe at different Reynolds numbers in the horizontal configuration are shown in Fig. 4 of our paper [37].

Three flow patterns, slug, churn, and annular flows, were recorded in the vertical riser at a distance of $100D^*$ downstream of the sharp bend for 338 flow conditions for air and water superficial velocities in the ranges listed in Table 2. Fig. 4a shows instantaneous snapshot of the patterns in the vertical pipe with D^*=21mm for j_L^*=0.279m/s and different j_G^*. The membrane flow structure, discovered by Milan *et al.* [20] in vertical downward flows, has been observed for the first time in the present study in the vertical upward flow downstream of the elbow as a result of the coalescence of the bubbles after their division through the elbow. Fig. 4b shows pictures of single and multiple membrane flow in the pipe with D^*=21mm for j_G^*=0.15m/s and different j_L^*. Up to four membranes were observed in a single air slug, often almost equally spaced along the vertical direction. Milan *et al.* [20] detected the membrane flow at a maximum water velocity of 0.41m/s, while we recorded the presence of these structures at higher water velocities, i.e., up to j_L^*=1.02m/s, which correspond to higher Reynolds numbers based on j_L^* because our three diameters are larger than Milan *et al.*'s, i.e., D^*=8.8mm.

Fig. 5 represents the observed flow patterns in the horizontal straight pipes on the Mandhane map [13], while Fig. 6 shows the patterns in the vertical straight pipes on the Hewitt-Roberts map [14]. We have chosen these maps to display our experimental data graphically because they were proposed to cover a wide range of pipe diameters, including ours. The comparison is better for the data for the vertical orientation in Fig. 6 than for the data for the horizontal orientation in Fig. 5.

In Appendix C a dimensional analysis based on the Π theorem shows that the patterns of an incompressible isothermal water-air flow can be expressed in scaled form in terms of only three non-dimensional parameters, i.e., the Reynolds number for water, $\mathcal{R}e_L = \dot{m}_L^*/(\mu_L^* D^*) = \rho_L^* j_L^* D^* \pi/(4\mu_L^*)$, the Reynolds number for air, $\mathcal{R}e_G = \dot{m}_G^*/(\mu_G^* D^*) = \rho_G^* j_G^* D^* \pi/(4\mu_G^*)$, and the Froude number, $Fr_L = \dot{m}_L^*/(\sqrt{g^*} D^{*5/2} \rho_L^*)$, where $\dot{m}_L^*, \dot{m}_G^*$ and μ_L^*, μ_G^* are the mass flow rates and viscosities of the two fluids, and g^* is the gravitational acceleration. The analysis demonstrates that only three parameters are necessary because for incompressible isothermal water-air flows

the other scaled parameters, the ratio of densities and the ratio of viscosities, are constant. In Appendix C we prove that the incompressibility condition holds as the density of air only changed by a maximum of about 3%. For a constant Froude number, a rigorous non-dimensional representation of incompressible constant-property water-air flow patterns is therefore a map in the $(\mathcal{R}e_G, \mathcal{R}e_L)$ plane.

We can then express the dimensional maps in Figs. 5 and 6 in terms of $\mathcal{R}e_L$ and $\mathcal{R}e_G$ by assuming that the effect of the Froude number is negligible. This hypothesis has been largely verified in the horizontal case at sufficiently high mass flow rates of both fluids because the stratified flow regime where gravity plays a decisive role does not occur [29]. This is the case of our experiments because all our data points are on the upper half of the horizontal-flow Mandhane map, as shown in Fig. 5. In the vertical-flow case, Spedding and Nguyen [43] (refer to the discussion of their figure 3 on page 785) showed that, in the Froude-number range of interest for our work, i.e., $0.5 \leq Fr_L \leq 2.5$, gravity has a very mild influence on the flow patterns, especially on the slug-flow regime.

To rescale the maps in terms of $\mathcal{R}e_L$, $\mathcal{R}e_G$, the velocities j_L^* and j_G^* at the boundaries between the regions distinguishing the flow patterns and the average value of our pipe diameters are used to compute $\mathcal{R}e_L$ and $\mathcal{R}e_G$. The rescaled Mandhane and Hewitt-Roberts maps are displayed in Figs. 7 and 8. The rescaled Mandhane map in Fig. 7 shows a slight improvement for the prediction across the boundary between the plug and slug regions as fewer plug-flow symbols fall in the slug-flow Mandhane region and no slug-flow symbols are confined in the strip dividing the two regions. This is instead the case in the dimensional Mandhane map of Fig. 5. In the rescaled Hewitt-Roberts map in Fig. 8, all the symbols fall more clearly within the predicted regions as they are more clustered together than in the dimensional map.

Fig. 9 shows the map obtained by Milan *et al.* [20] to identify the regions in the parameter space where the membrane flow was observed for vertical downward flow. Because our pipe diameters are different from Milan *et al.*'s, we show the map in non-dimensional form. In line with the discussion of Fig. 4b, almost all the flow conditions for which we detected the membrane flow lie in a range of $\mathcal{R}e_L$ that is higher than Milan *et al.* [20]'s. At such high $\mathcal{R}e_L$, Milan *et al.* [20] did not observe the membrane flow.
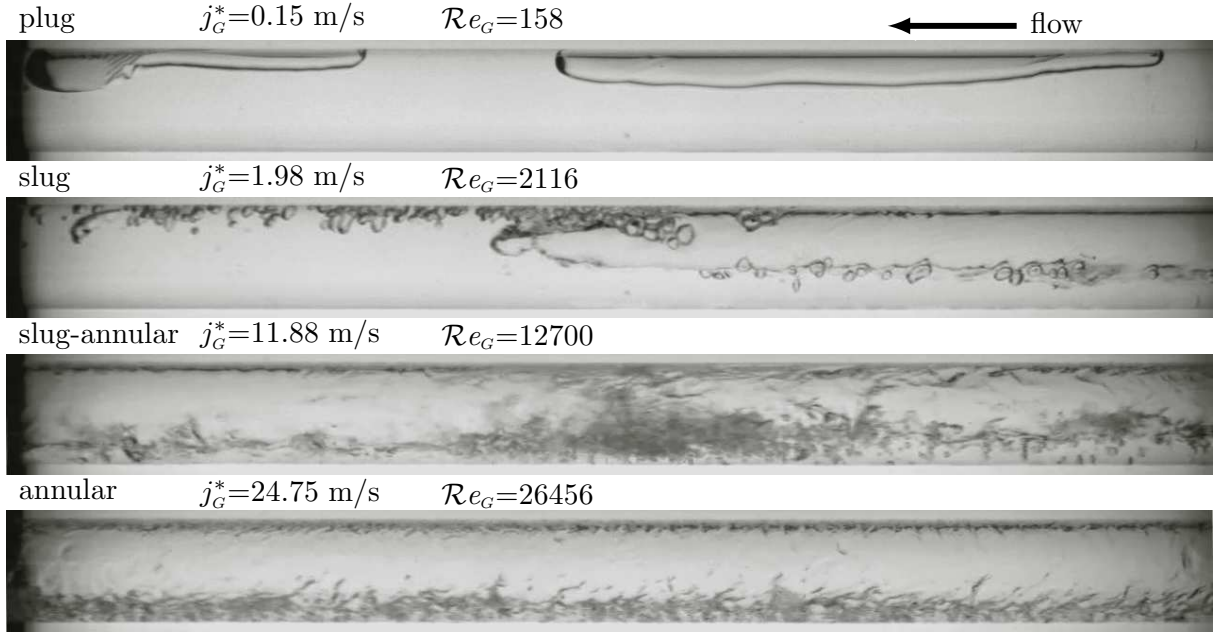
Figure 3: Patterns upstream of the bend in the horizontal configuration for D^*=21mm, j_L^*=0.396m/s, $\mathcal{R}e_L=\rho_L^* j_L^* D^* \pi/(4\mu_L^*)$=7464 and different j_G^*. The Reynolds number for air is defined as $\mathcal{R}e_G=\rho_G^* j_G^* D^* \pi/(4\mu_G^*)$. The densities of the fluids are ρ_k^* and the dynamic viscosities are μ_k^*.
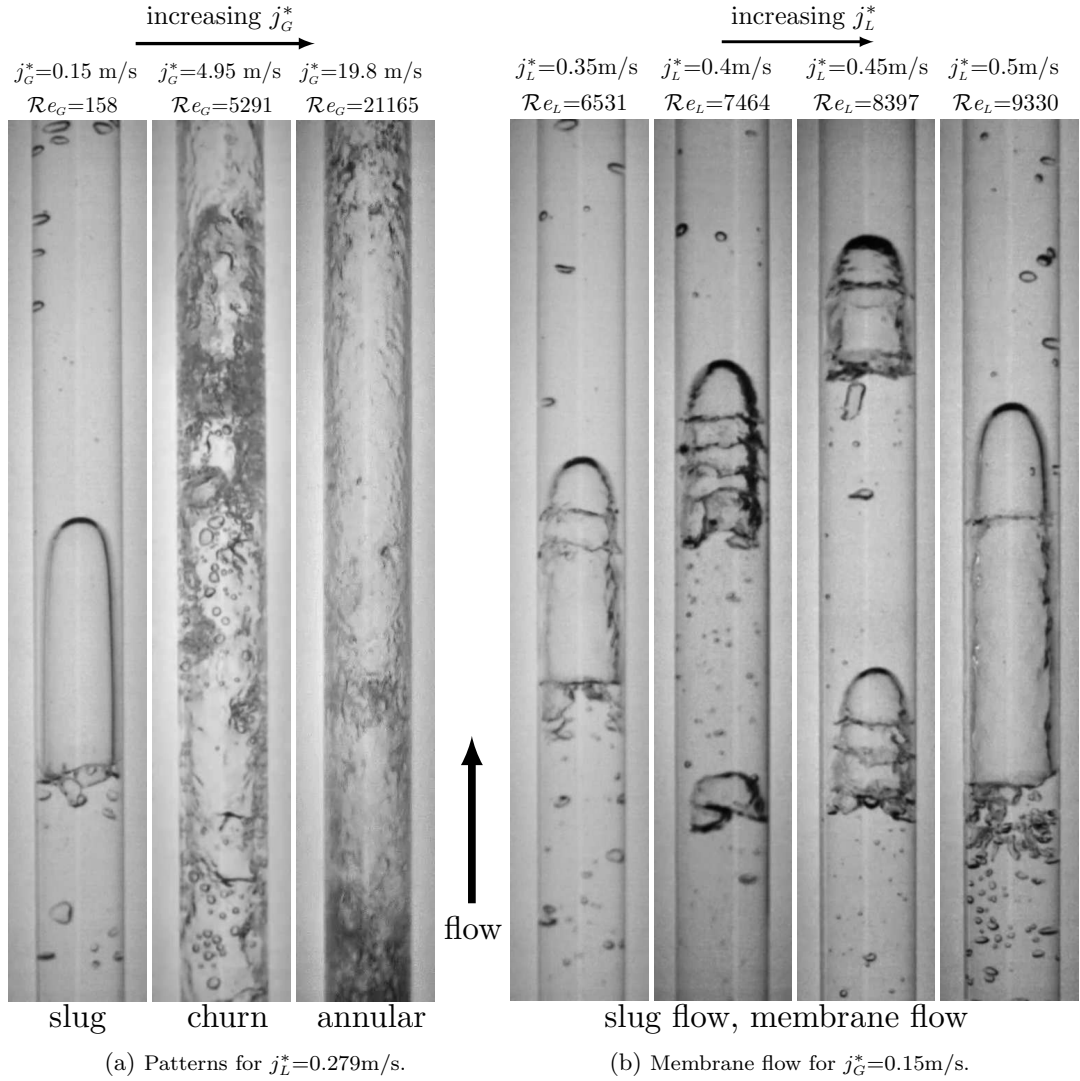

(a) Patterns for j_L^*=0.279m/s.

(b) Membrane flow for j_G^*=0.15m/s.

Figure 4: Flow patterns in vertical pipe section downstream of the sharp bend for D^*=21mm, (a) $\mathcal{R}e_L$=5598 and (b) $\mathcal{R}e_G$=159.

7
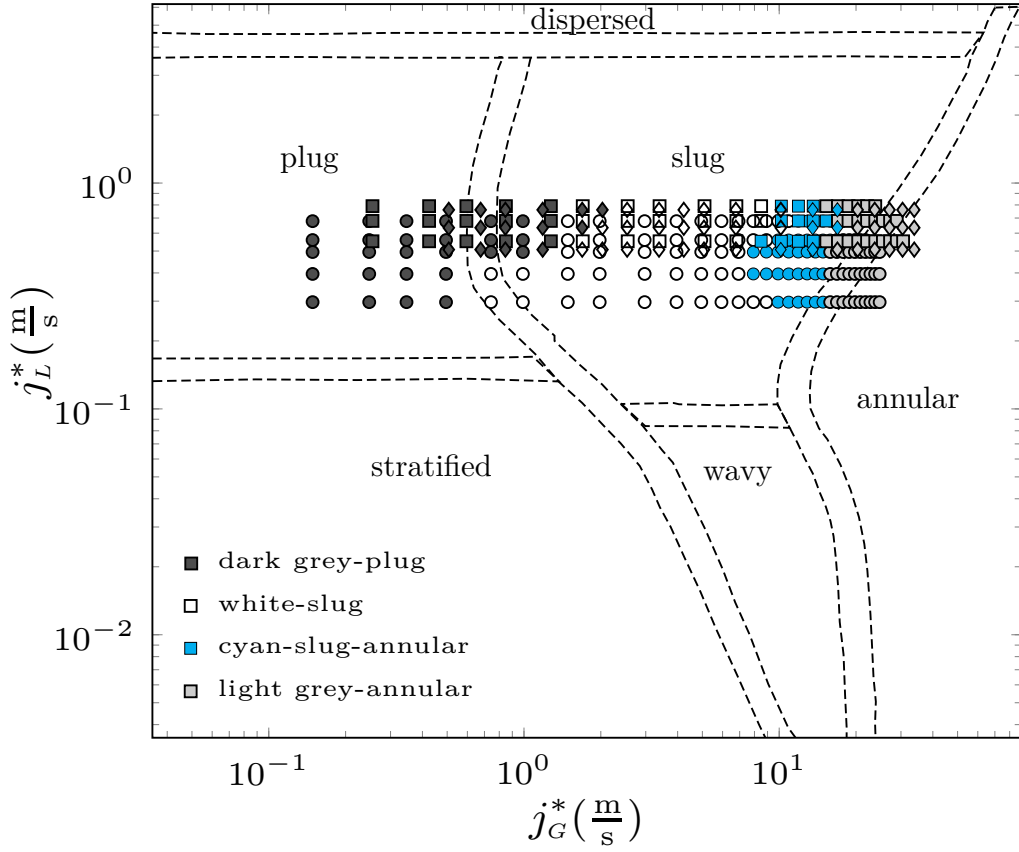
Figure 5: Comparison between the observed flow patterns in horizontal pipe sections, represented by the colours of the symbols, with the prediction given by the Mandhane map [13] for D^*=21mm ($\circ$), D^*=16mm ($\square$), and D^*=11mm ($\diamond$).
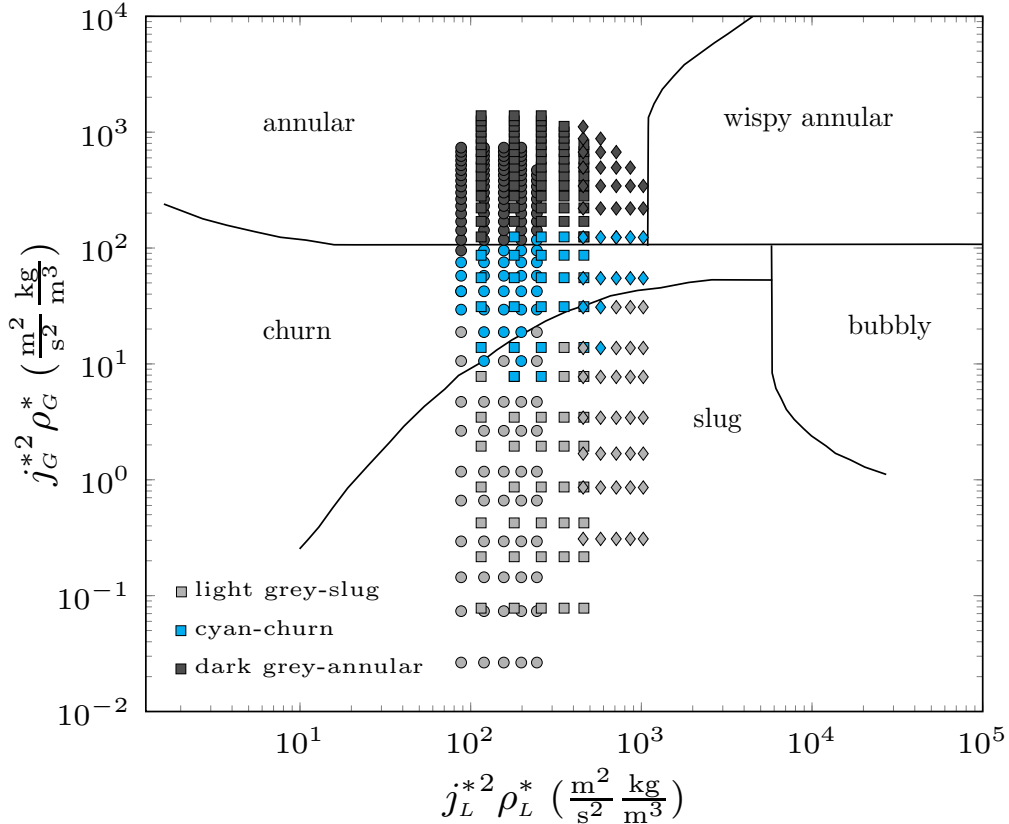
Figure 6: Comparison between the observed flow patterns in the vertical straight pipe sections with the prediction given by the Hewitt-Roberts map [14] for D^*=21mm ($\circ$), D^*=16mm ($\square$), and D^*=11mm ($\diamond$).
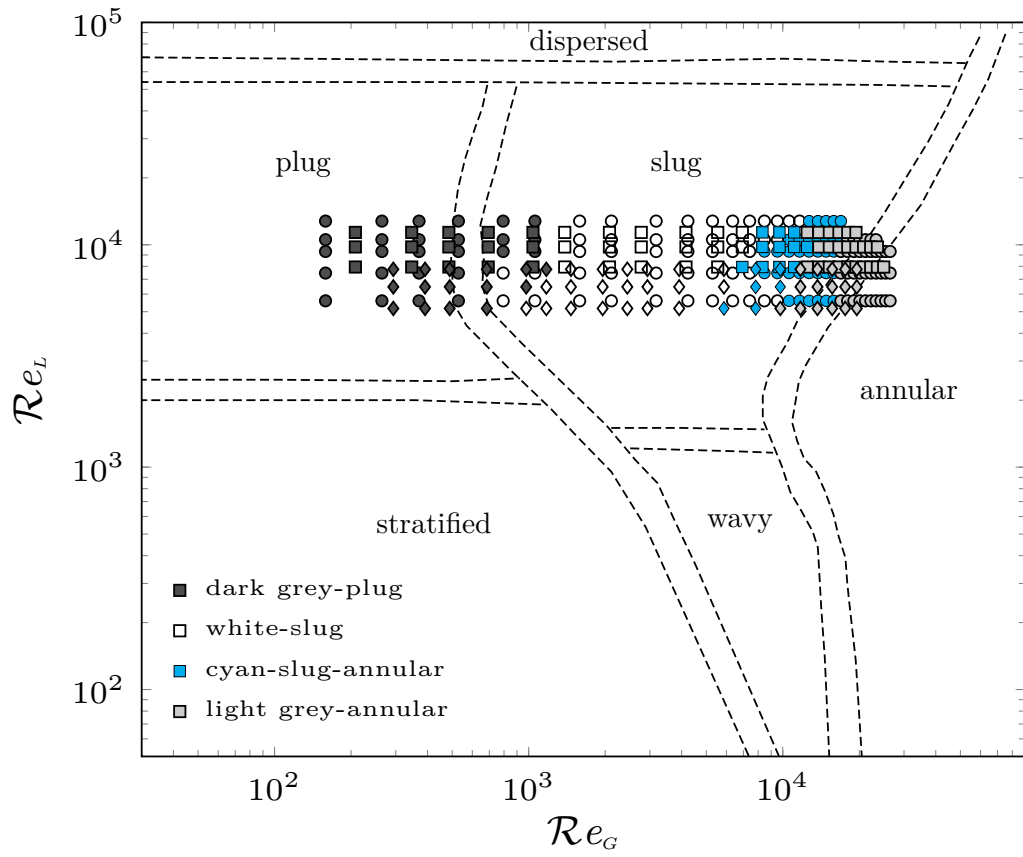
Figure 7: Comparison between the observed flow patterns, represented by the colours of the symbols, in horizontal straight pipes with the prediction given by the rescaled Mandhane map [13], for D^*=21mm (○), D^*=16mm (□), and D^*=11mm (◇).
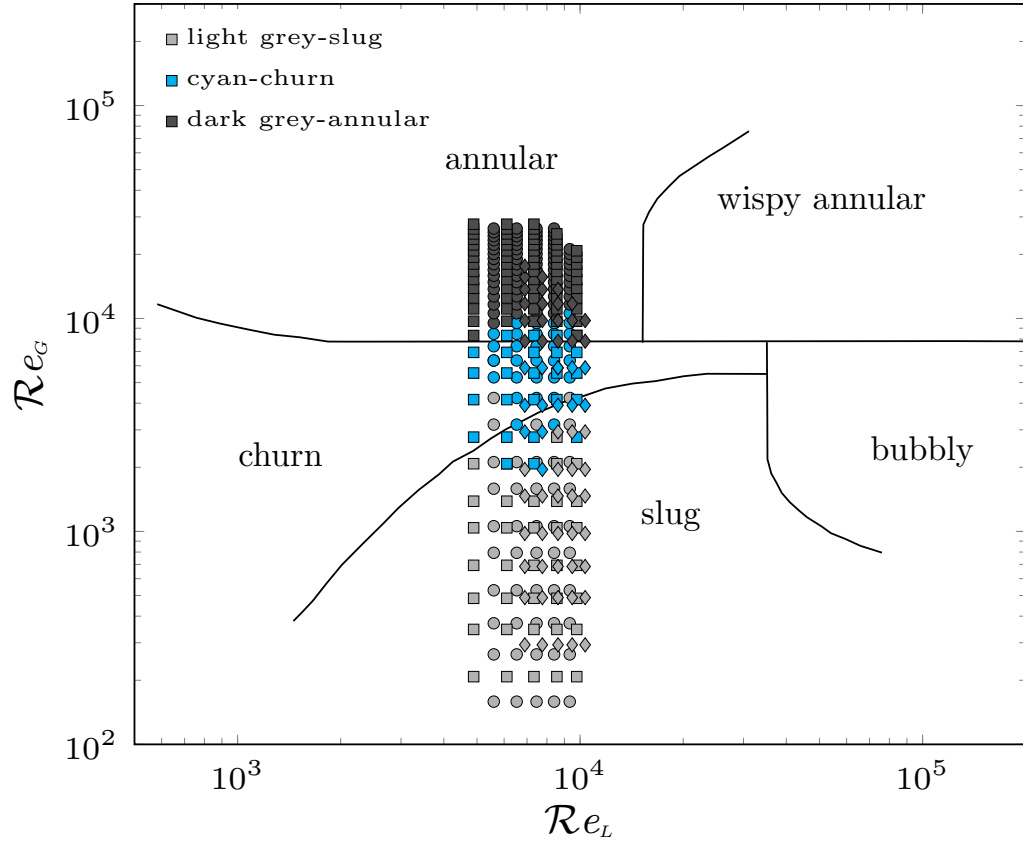

Figure 8: Comparison between the observed flow patterns, represented by the colours of the symbols, with the non-dimensional Hewitt-Roberts map [14], for D^*=21mm (○), D^*=16mm (□), and D^*=11mm (◇).
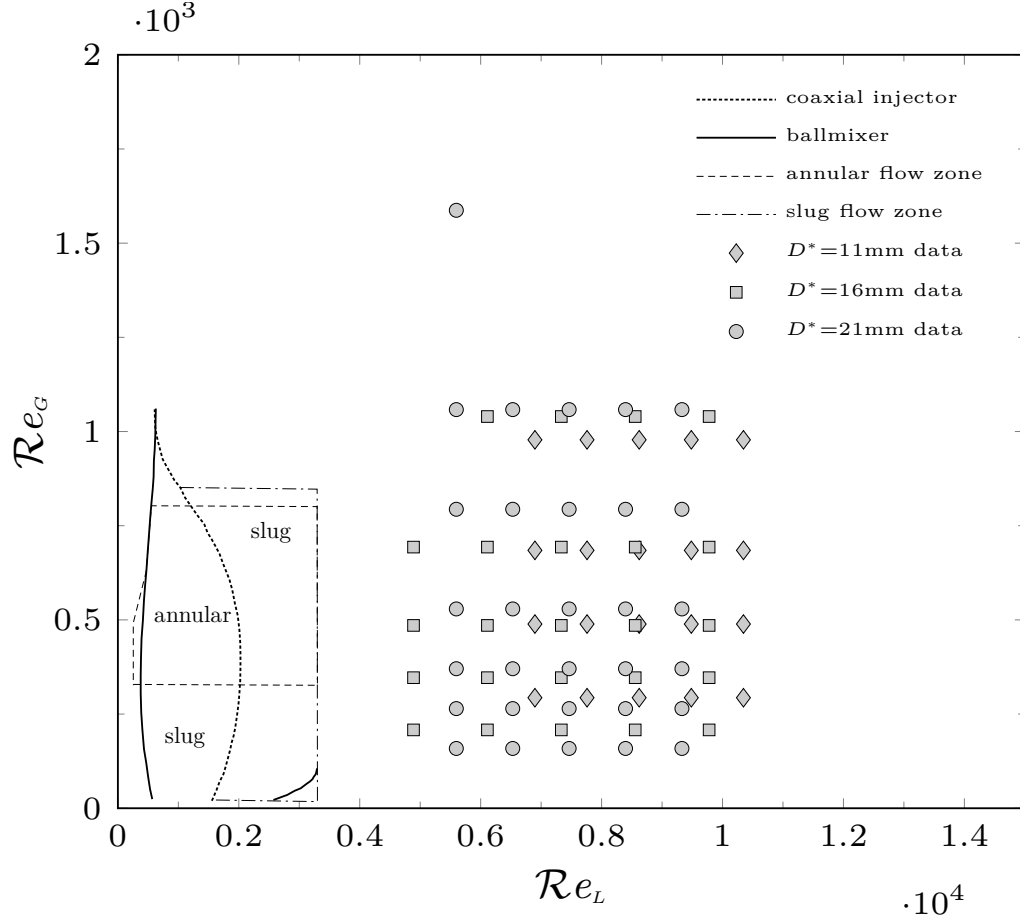
Figure 9: Comparison between the experimental data and non-dimensional Milan *et al.*'s [20] membrane flow map.

3.1.2. Flow patterns across the mitre elbow

The two-phase flow patterns through the mitre elbows have been investigated visually to document the behaviour of the flow regimes through the sharp bend caused by the interaction of different forces, like the centrifugal force, the gravity force, and the buoyancy force. When the elbow was positioned vertically, we investigated the horizontal to vertical upward flow, which is one of four possible flow orientations for this geometry, the others being the horizontal to vertical downward flow, the vertical upward to horizontal flow, and the vertical downward to horizontal flow.

Horizontal orientation

For $\mathcal{R}e_G$<200 in the horizontal orientation, the plug flow is not affected by the elbow due to the balance between the secondary flow and the gravitational effects. The elongated air bubbles, observed for 200<$\mathcal{R}e_G$<3000 in plug and slug flows, divide into two or more bubbles as the flow passes through the elbow, as shown in Fig. 10 in the pipe with D^*=21mm. The disruption of the bubbles is caused by the flow separation and the intense secondary flow across the elbow. The divided bubbles often merge downstream of the sharp bend to recover the unperturbed regimes upstream of the elbow as the centrifugal force vanishes downstream of the bend, similar to the results of Chen *et al.* [16] in horizontal return bends. At higher air velocities, 3000<$\mathcal{R}e_G$<20000, slug and slug-annular flows suddenly become annular downstream of the sharp bend due to the centrifugal effects dominating over the gravitational effects. This annular flow downstream of the elbow is different from the annular flow in straight pipes because it is swirling as the water layers move in rotational motion around the core of air flow and along the pipe periphery, while the wall-attached layer in straight pipe annular flow moves parallel to the pipe axis. The flow then recovers its original pattern approximately $60D^*$ downstream of the bend. Fig. 11 shows the flow change from slug to swirling annular through a D^*=21mm horizontal elbow. This phenomena was reported by Chen *at al.* [16] and Wang *et al.* [11, 17] in horizontal 180° bends at superficial velocities larger than ours because the secondary flow in our 90° mitre elbows is more intense than that in round bends for similar flow conditions.

For $\mathcal{R}e_G$>20000 the flow upstream of the elbow is annular and has a thick bottom water layer. Downstream of the elbow it is still annular but it is characterized by a constant-thickness axisymmetric water layer because

the inertia of the secondary flow and the centrifugal force dominate over the gravitational effects. Like in the case in Fig. 10, the water layers of the annular flow downstream of the elbow swirl around the pipe periphery before the flow recovers to the standard, non-rotating annular regime about $60D^*$ downstream of the sharp bend. Fig. 12 illustrates this phenomenon through the D^*=21mm horizontal elbow for different flow conditions.

Two-phase flow patterns through horizontal mitre elbows are represented for the first time in terms of the non-dimensional Mandhane map [13], shown in Fig. 13. This novel representation is useful because it visually combines information on the flow regime upstream of the elbow, given by the location of the symbols in the Mandhane regions, with the information on the change of the flow regimes as the fluids move across the elbow, denoted by the colour of the symbol.

Figure 10: Bubble division and coalescence in the horizontal elbow with D^*=21mm, $\mathcal{R}e_L$=5598 and $\mathcal{R}e_G$=1058.
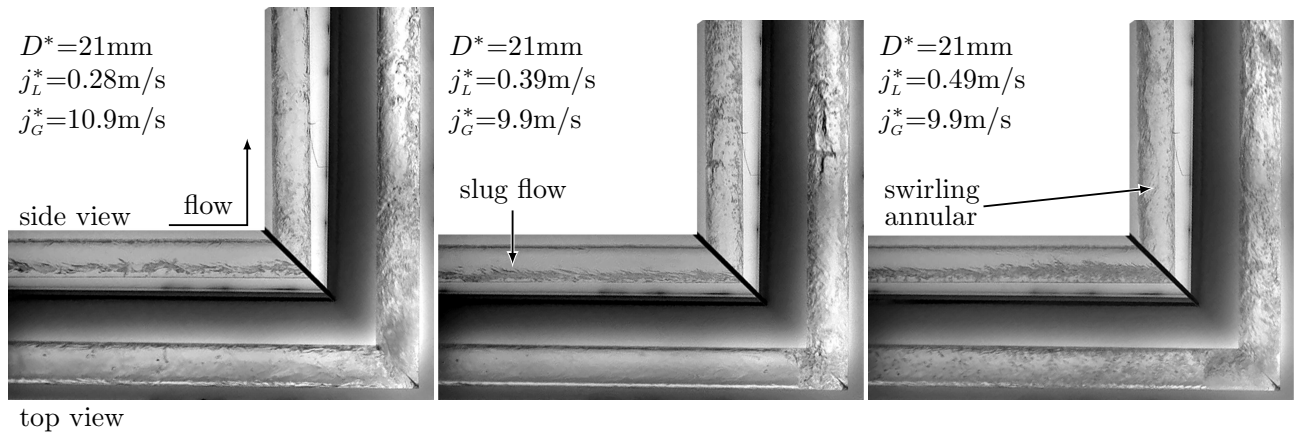

Figure 11: Change from slug flow to swirling annular flow across the horizontal elbow with D^*=21mm. Left photo: $\mathcal{R}e_L$=5598 and $\mathcal{R}e_G$=11641. Middle photo: $\mathcal{R}e_L$=7464 and $\mathcal{R}e_G$=11641. Right photo: $\mathcal{R}e_L$=9330 and $\mathcal{R}e_G$=10582.
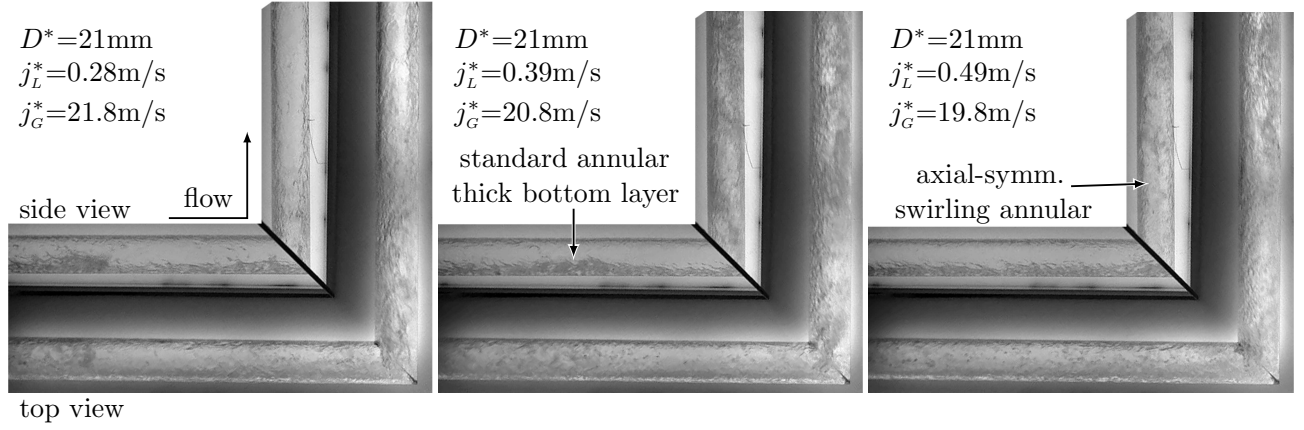
Figure 12: Change from annular flow to swirling annular flow across the horizontal elbow with D^*=21mm. Left photo: $\mathcal{R}e_L$=5598 and $\mathcal{R}e_G$=23281. Middle photo: $\mathcal{R}e_L$=7464 and $\mathcal{R}e_G$=22223. Right photo: $\mathcal{R}e_L$=9330 and $\mathcal{R}e_G$=21165.
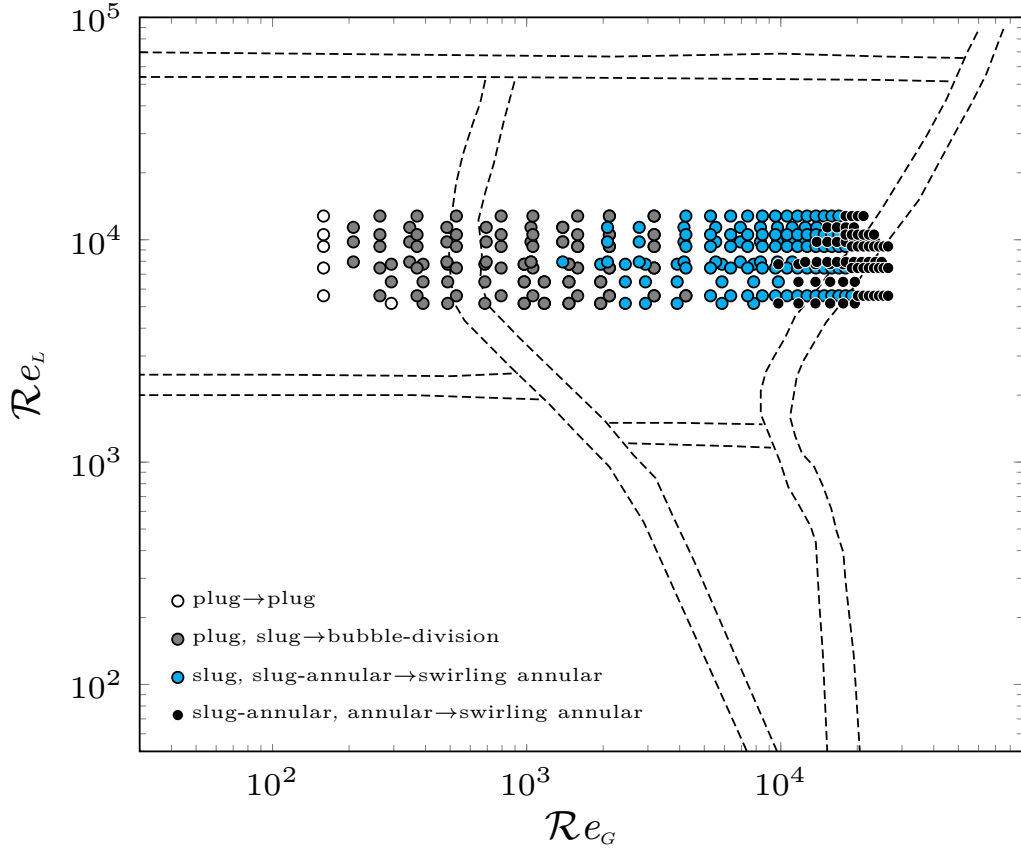

Figure 13: Representation of the two-phase flow patterns through the mitre elbows in the horizontal orientation on the non-dimensional Mandhane map [13]. The flow regime upstream of the elbow are denoted by the location of the symbols in the Mandhane regions, while the flow regimes downstream of the sharp bend are indicated by the colour of the symbol.

Horizontal to vertical upward orientation

For $\mathcal{R}e_G$<2000, the intermittent flow patterns (plug and low-j_G^* slug) entering the horizontal part of the elbow change to slug flow in the riser downstream of the sharp bend due to the effect of gravity. In the upward flow, a liquid-phase reverse downward flow may occur for these flow conditions. This reverse water flow splits the air slugs into two or more bubbles downstream of the bend. The divided bubbles then coalesce, often resulting in a membrane flow structure, as shown in Fig. 14 in the vertical elbow with D^*=21mm at different times. The phenomenon of flow reversal and bubble separation were reported by Hsu *et al.* [19] in 90° round elbows and Wang *et al.* [18] in 180° bends at velocities higher than ours because the secondary flow, which is the main cause for this phenomenon, increases with the decrease of curvature radius of the elbow for the same flow conditions, as also mentioned by Wang and Mayinger [44] and Wang *at al.* [17].

For 1000 < $\mathcal{R}e_G$<3000, the slug flow upstream of the elbow remains as such in the vertical pipe downstream of the sharp bend, but it changes character. In the horizontal pipe upstream of the bend, the air slugs occur in the top part of the pipe while thin water layers appear at the bottom. Downstream of the elbow in the vertical pipe, the air slugs move in the centre of the pipe while thin liquid films occur between the slugs and the pipe wall. At higher j_G^*, i.e., for 3000<$\mathcal{R}e_G$<10000, the slug flow converts to churn flow through the elbow, as shown in Fig. 15 for the elbow of D^*=21mm at j_L^*=0.297m/s.

At higher j_G^*, i.e., for $\mathcal{R}e_G$>10000, the slug and slug-annular flows upstream of the sharp bend in the horizontal configuration change to swirling annular as the fluids pass through the elbow due to the centrifugal force and the secondary-flow effects dominating over the gravitational effects, similar to the results of Wang *et al.* [18] in vertical 180° round elbows. Like for the elbow in the horizontal configuration, the water layers of the swirling annular flow downstream of the elbow rotate around the pipe periphery before the flow establishes itself back to the standard annular regime at a distance of about 60D^* downstream of the sharp bend.

The annular flow enters the horizontal leg of the vertical elbow with a thicker water layer in the lower part of the pipe and changes to a swirling annular flow with an axisymmetric water-layer thickness downstream of the bend, as shown in Fig. 17 for the D^*=21mm elbow.

Similar to the map of Fig. 13, the water-air flow patterns through the elbows in the horizontal to vertical upward position are represented on the rescaled Mandhane map [13] of Fig. 18 for the first time.
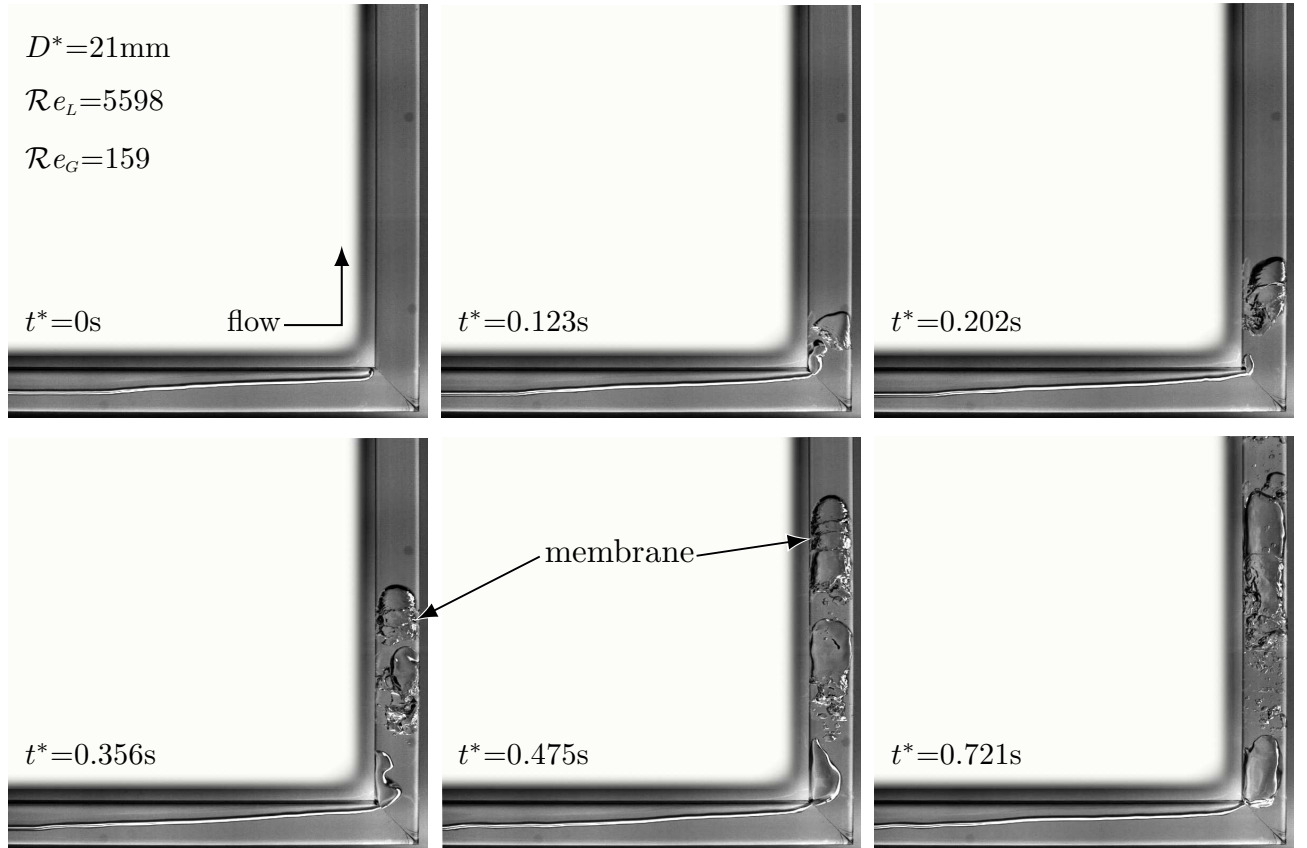

Figure 14: Change from plug flow to slug flow due to separation of bubbles across the elbow for D^*=21mm, j_L^*=0.297 m/s, j_G^*=0.15m/s, $\mathcal{R}e_L$=5598 and $\mathcal{R}e_G$=159.
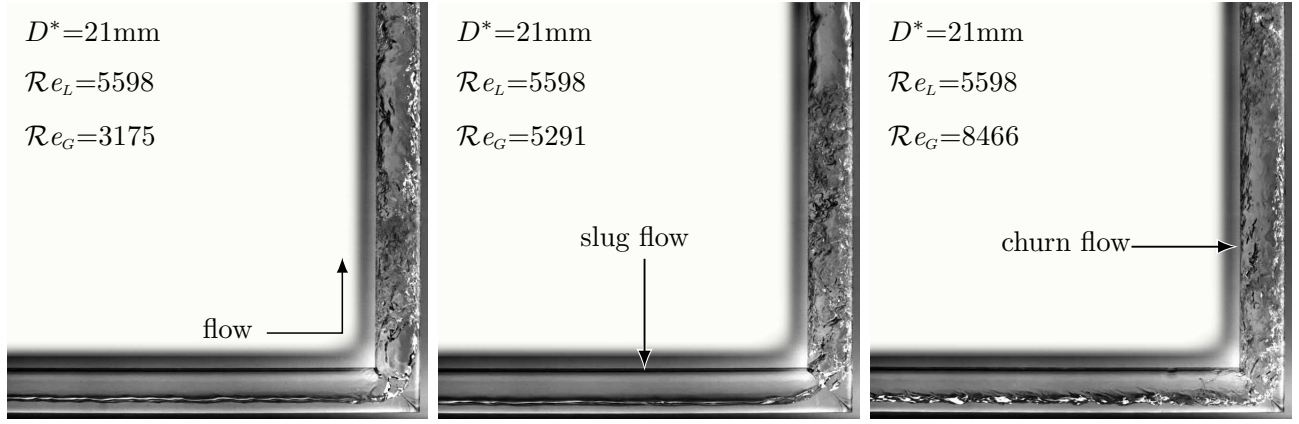
Figure 15: Change from slug flow to churn flow through the vertical elbow for D^*=21mm, j_L^*=0.297 m/s, and different j_G^*. Left photo: $\mathcal{R}e_L$=5598 and $\mathcal{R}e_G$=3175. Middle photo: $\mathcal{R}e_L$=5598 and $\mathcal{R}e_G$=5291. Right photo: $\mathcal{R}e_L$=5598 and $\mathcal{R}e_G$=8466.
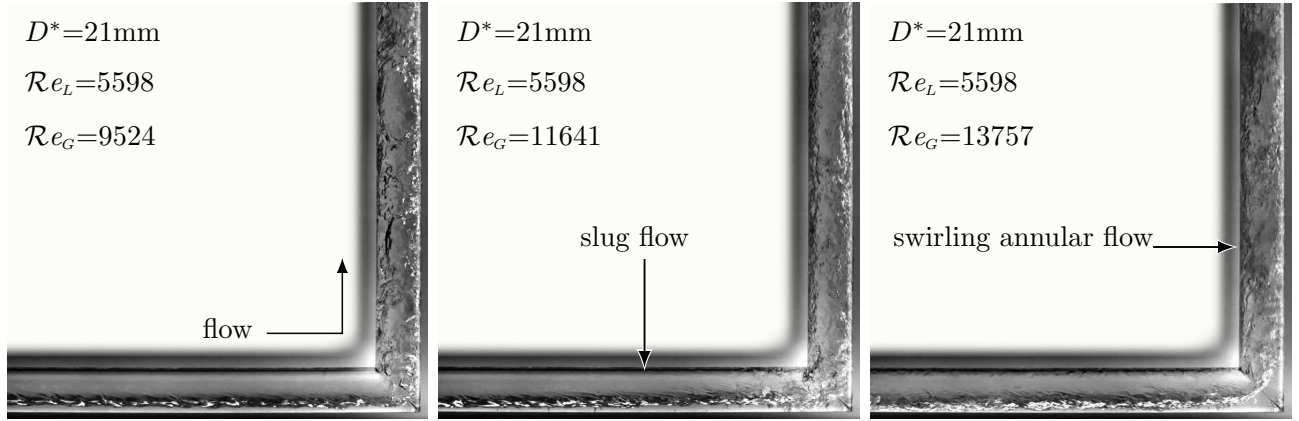

Figure 16: Change from slug flow to swirling annular flow through the horizontal to vertical elbow for D^*=21mm, j_L^*=0.297 m/s, and different j_G^*. Left photo: $\mathcal{R}e_L$=5598 and $\mathcal{R}e_G$=9524. Middle photo: $\mathcal{R}e_L$=5598 and $\mathcal{R}e_G$=11641. Right photo: $\mathcal{R}e_L$=5598 and $\mathcal{R}e_G$=13757.
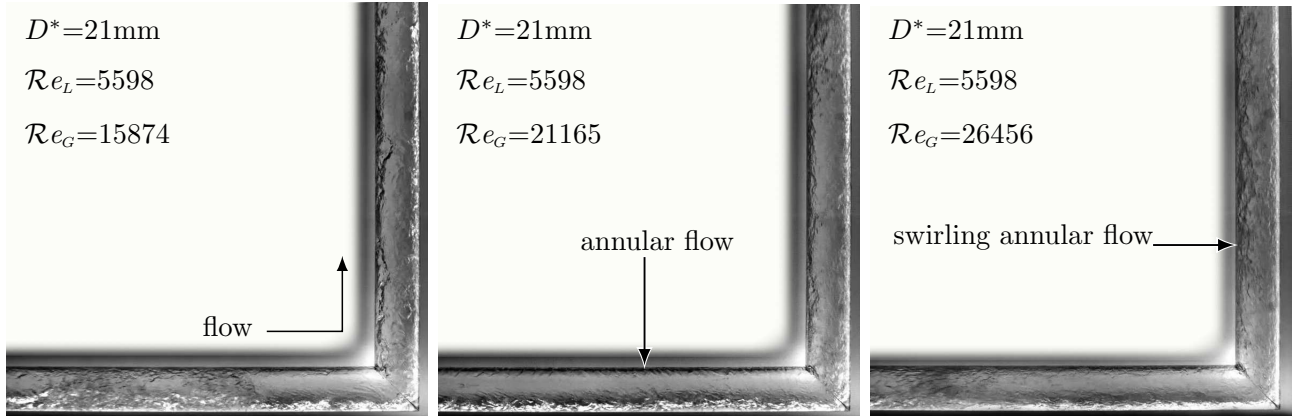

Figure 17: Standard annular flow change to swirling annular flow through the horizontal to vertical elbow with upward flow for D^*=21mm, j_L^*=0.297m/s and different j_G^*. Left photo: $\mathcal{R}e_L$=5598 and $\mathcal{R}e_G$=15874. Middle photo: $\mathcal{R}e_L$=5598 and $\mathcal{R}e_G$=21165. Right photo: $\mathcal{R}e_L$=5598 and $\mathcal{R}e_G$=26456.
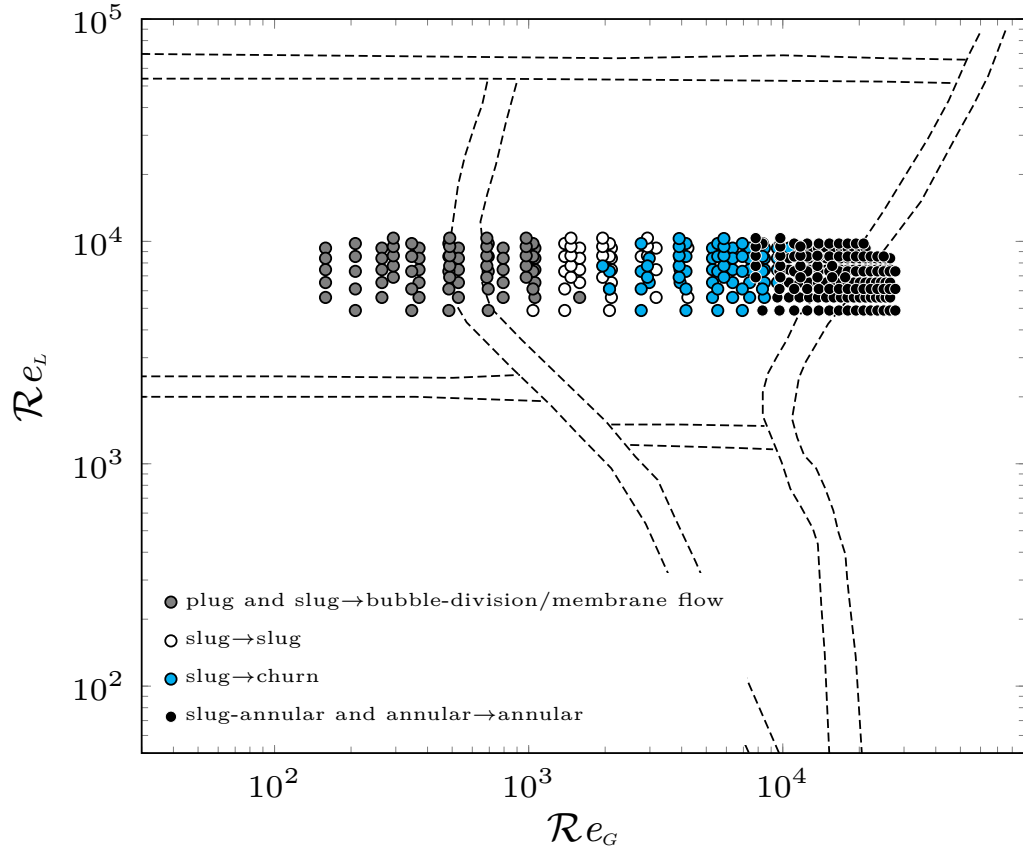
Figure 18: Representation of the two-phase flow patterns through the mitre elbows in the horizontal to vertical upward orientation on the non-dimensional Mandhane map [13]. Like in Fig. 13, the flow regime upstream of the elbow are denoted by the location of the symbols in the Mandhane regions, while the flow regimes downstream of the sharp bend are indicated by the colour of the symbol.

3.2. Analysis of pressure drop

3.2.1. Pressure drop along the straight pipes

For the two-phase flow study, it was imperative to ensure first that the our measured single-phase Darcy friction factor agreed with correlations available in the literature to verify the experimental measurements. Figure 19 shows the comparison between our experimental single-phase water pressure-drop measurements along the straight portions of the pipe upstream of the mitre elbows in terms of the friction factor $\mathcal{C}_L = 2\Delta p^* D^* / \left(\Delta l^* \rho_L^* j_L^{*2} \right)$ as a function of the Reynolds number, which was defined as $\mathcal{R}e_L = \rho_L^* j_L^* D^* / \mu_L^*$ for this single-phase analysis. An excellent agreement was found with well-known correlations.

For the two-phase flow, the distance upstream of the elbow where the flow starts to be affected by the elbow and the distance downstream of the bend after which the presence of the elbow is not influential were measured. The flow recovery length was $60D^*$ downstream of the bend and the upstream perturbation distance was $32.5D^*$ upstream of the elbow. Like for the single-phase study documented in our paper [35], the pressure produced by the water-air flow was axisymmetric around the pipe periphery at all the tested positions. These measurements agree with the result by Lima and Thome for the two-phase refrigerant flow through horizontal $180°$ round elbows [12].

In Appendix A, Fig. A.26 shows a comparison between our pressure-drop data in straight pipes in the horizontal and vertical configurations and the predictions by the models proposed by Lockhart & Martinelli [2], Chisholm [3], and Muller & Heck [6], which do not include the effects of the flow patterns. The data are not predicted well by the models. The deviation between the experimental data and the predicted values increases as the pressure drop increases. The Lockhart-Martinelli model [2] leads to a better agreement with the experimental data than the other two models. At very small pressure drops ($\Delta p^*/\Delta l^* < 2500$Pa/m), the Lockhart-Martinelli [2] and the Muller-Heck [6] models predict the experimental data with good agreement. At higher pressure drops, the Muller-Heck model [6] gives a deviation from the experimental data that is much larger than the other two models. The deviation between the models and the experimental data was lower in the vertical case than in the horizontal case.

In Appendix C the dimensional analysis shows that the scaled frictional pressure drop of an incompressible isothermal water-air flow can be scaled as

$$\mathcal{C}_L = \frac{\Delta p^*}{\Delta l^*}\bigg|_{\mathrm{f}} \frac{D^{*5}\rho_L^*}{\dot{m}_L^2} \tag{4}$$

and expressed as a function of the three non-dimensional parameters, i.e., $\mathcal{C}_L = \mathcal{C}_L\left(\mathcal{R}e_L, \mathcal{R}e_G, Fr_L\right)$.

In Fig. 20 the two-phase $\mathcal{C}_L$ data for the horizontal straight pipe upstream of the elbow in the present work and the data of Spedding and Benard [45] and Kim *et al.* [46] show excellent collapse when $\mathcal{C}_L\mathcal{R}e_G^{\alpha}$ is plotted as a function of $(\mathcal{R}e_L/\mathcal{R}e_G)^{\beta}$. A least-square fit analysis gives α=0.3 and β=0.5. The effect of Froude number is negligible in this range of parameters, as expected in the horizontal case. The excellent scaling of the data is independent of the flow patterns, which are represented by different colours in Fig. 20.

Figure 21 represents the two-phase $\mathcal{C}_L$ data for the vertical straight pipe downstream of the elbow and the experimental data by Tang *et al.* [47]. The collapse of data scaled in the form $\mathcal{C}_L\mathcal{R}e_G^{\alpha}$ as a function of $(\mathcal{R}e_L/\mathcal{R}e_G)^{\beta}$ (α=0.85 and β=0.5) is also very good, although the scatter of some data is larger than in the horizontal configuration because of the effect of Fr_L. This is also expected because gravity plays a non-negligible role in the vertical configuration. To clarify the effect of Fr_L the scaled pressure-drop data for the vertical-pipe case of Fig. 21 is coloured by Fr_L in Fig. 22. The effect of Fr_L is most intense in the range $0.45 < (\mathcal{R}e_L/\mathcal{R}e_G)^{0.5} < 1.25$, causing scatter in the experimental data in the region between the churn and annular flows.

Figs. 21 and 22 show that the frictional pressure drop may have negative values in the churn and annular regimes because the static pressure drop due to gravity overcomes the frictional effect, a phenomenon due to reversed liquid flow at the pipe surface and reported, amongst others, by Spedding's group [48, 49, 45] and by Liu's group [50, 47, 51] in vertical pipe flows. The negative-friction data are highlighted by the hatched area in Fig. 22. Note that the range of parameters for which the negative friction occurs falls within the range where the effect of Froude number is significant.

New pattern-based correlations are proposed by using multiple regression tool in Statgraphics 16.1 [52] to fit the experimental data of the frictional pressure drop in horizontal and vertical pipes. The correlations in this section and in §3.2.2 are also valid for any two fluids with the same viscosity and density ratios as the water-air ratios and flowing in the ranges of Reynolds numbers stated next to each equation. For the horizontal case the following correlation is proposed for intermittent (plug and slug) flows:

$$\mathcal{C}_L\mathcal{R}e_G^{0.3} = 2.914\left(\frac{\mathcal{R}e_L}{\mathcal{R}e_G}\right)^{-0.89} - 0.0075, \qquad \left(\frac{\mathcal{R}e_L}{\mathcal{R}e_G}\right)^{0.5} > 1. \tag{5}$$

For slug-annular and annular flows in the horizontal case, we propose the following correlation:

$$\mathcal{C}_L \mathcal{R}e_G^{0.3} = 1.54 \left(\frac{\mathcal{R}e_L}{\mathcal{R}e_G}\right)^{-1.71} + 1.554, \qquad \left(\frac{\mathcal{R}e_L}{\mathcal{R}e_G}\right)^{0.5} < 1. \tag{6}$$

Correlations (5) and (6) fit the scaled experimental data with $\mathcal{E} = 2.4\%$ and $\mathcal{E} = 7.8\%$, respectively. The following correlation is proposed to fit the pressure-drop data for all flow patterns in the horizontal configuration:

$$\mathcal{C}_L \mathcal{R}e_G^{0.3} = 2.607 \left(\frac{\mathcal{R}e_L}{\mathcal{R}e_G}\right)^{-1.35} + 0.23, \qquad 0.4 < \left(\frac{\mathcal{R}e_L}{\mathcal{R}e_G}\right)^{0.5} < 8. \tag{7}$$

Correlation (7) fits our experimental data with $\mathcal{E} = 15\%$ and the data of Spedding and Benard [45] and Kim *et al.* [46] with $\mathcal{E} = 32\%$. The frictional pressure-drop data for vertical upward churn and annular flows are correlated as follows:

$$\mathcal{C}_L \mathcal{R}e_G^{1.35} = 41290 \left(\frac{\mathcal{R}e_L}{\mathcal{R}e_G}\right)^{-1.45} - 7405, \qquad 0.35 < \left(\frac{\mathcal{R}e_L}{\mathcal{R}e_G}\right)^{0.5} < 1.5, \tag{8}$$

Correlation (8) fits 70% of our scaled experimental data with $\mathcal{E} = 25\%$. Due to the scatter in the pressure drop data in vertical pipes, we could not correlate these data with acceptable error for the whole range of flow patterns. However, we propose a new correlation to fit the experimental data for $Fr_L > 1$ as:

$$\mathcal{C}_L \mathcal{R}e_G^{1.35} = 29330 \left(\frac{\mathcal{R}e_L}{\mathcal{R}e_G}\right)^{-2.26} - 60.3, \qquad \left(\frac{\mathcal{R}e_L}{\mathcal{R}e_G}\right)^{0.5} > 0.35. \tag{9}$$

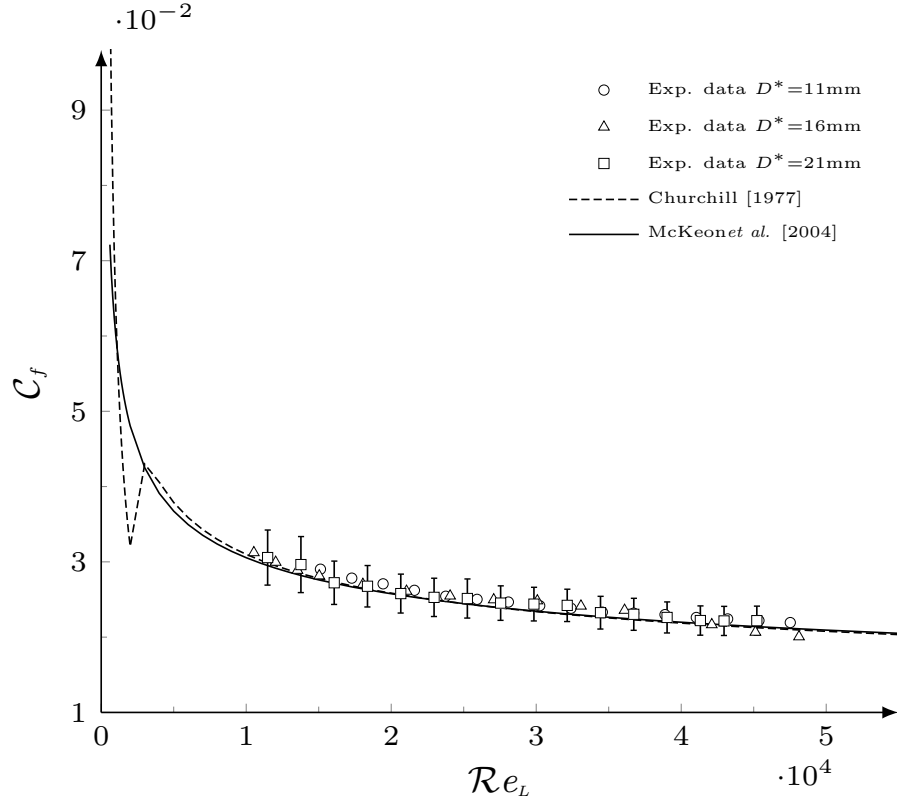Correlation (9) fits 60% of the experimental data for $Fr_L > 1$ with $\mathcal{E} = 19\%$.

Figure 19: Comparison between the single-phase friction factor $\mathcal{C}_f$ along straight pipes and two correlations.
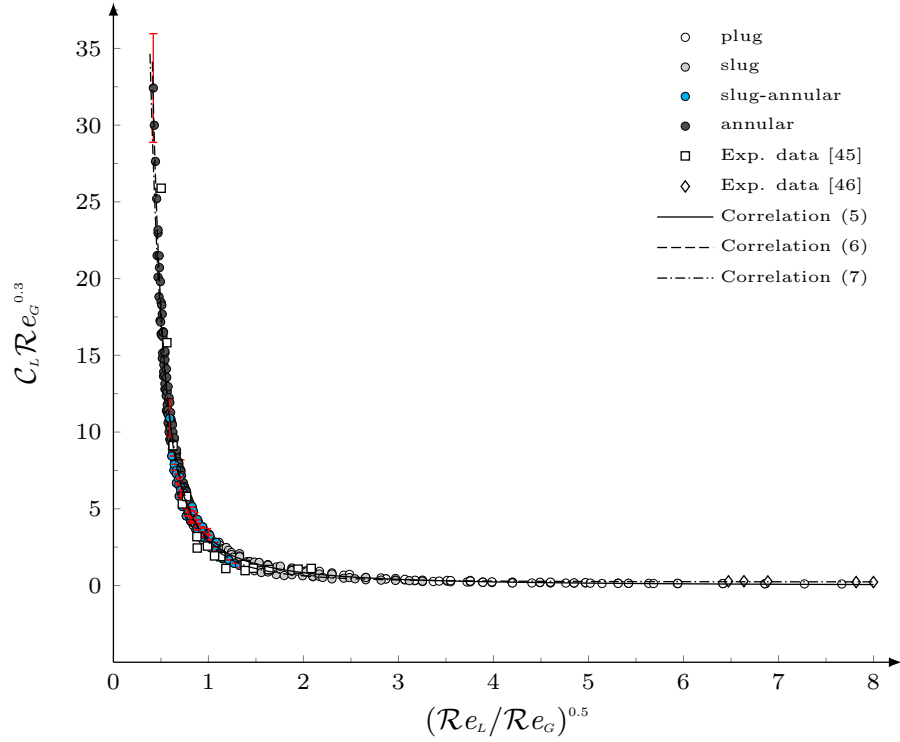

Figure 20: Scaled two-phase pressure drop in horizontal pipes. Error bars are shown in red in this figure and in the following ones.
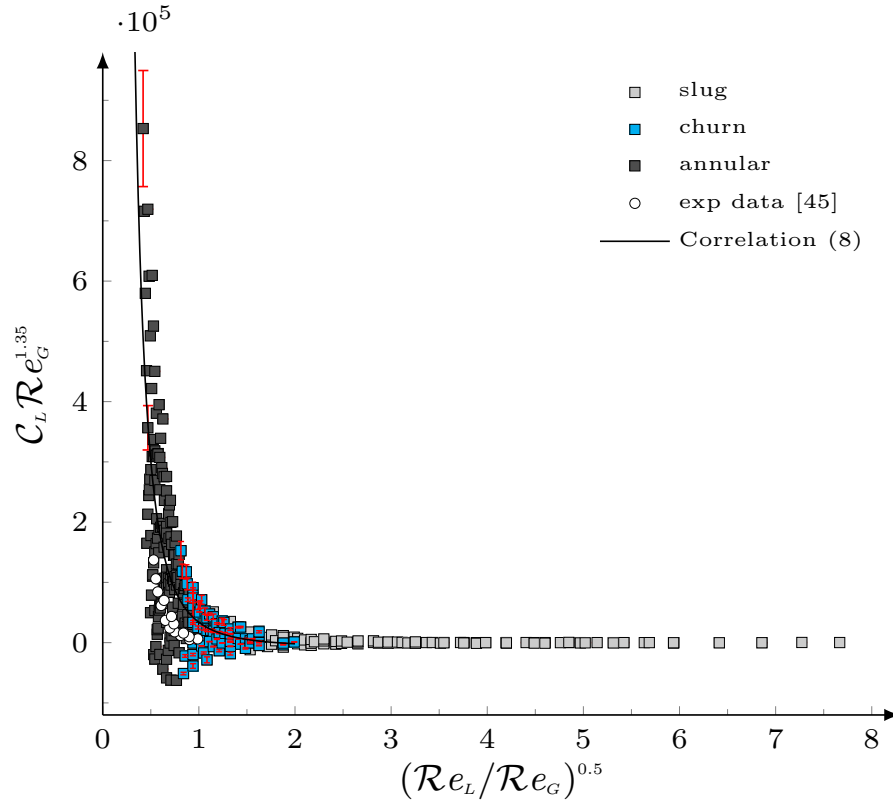
18

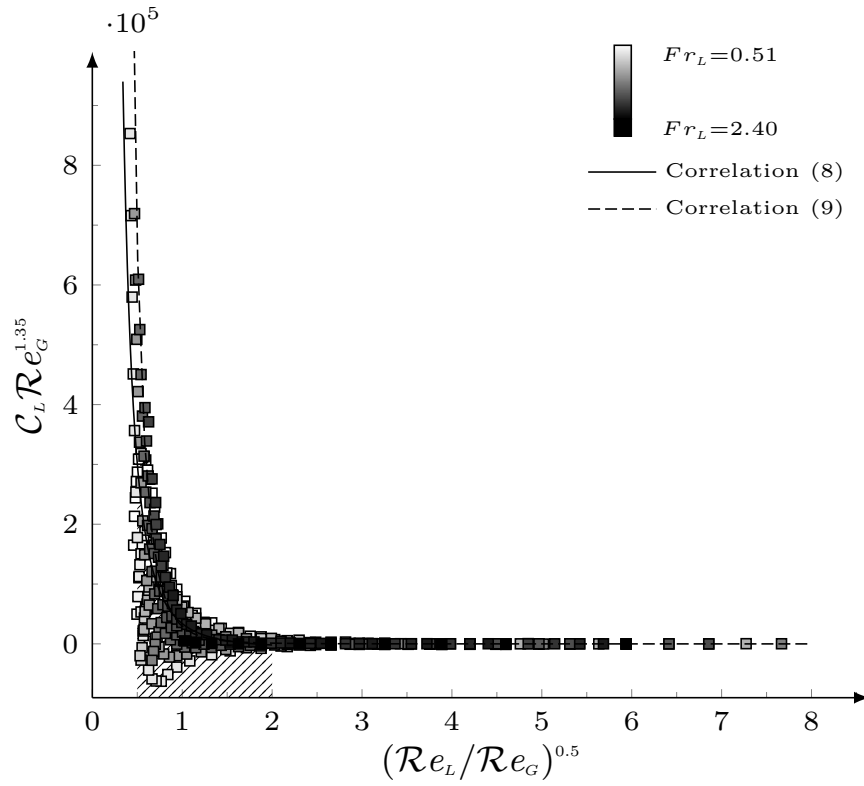Figure 21: Scaled two-phase pressure drop in vertical pipes.

Figure 22: Scaled two-phase pressure drop in vertical pipes coloured by Fr_L.

3.2.2. Pressure drop across the mitre elbows

Fig. B.28 shows the comparison between our experimental data for the flow across the horizontal and horizontal to vertical mitre elbows for a wide range of flow conditions, listed in Tables 1 and 2, and the prediction given by the models proposed by Chisholm [7] and Sookprasong *et al.* [10]. These models severely overpredict the pressure drops, especially at high flow rates. For both orientations, the deviation increases as the pressure drop grows. This error is expected because these correlations model the frictional pressure drop across round elbows. These models do not include the influence of the flow patterns on the pressure drop [9, 1, 28, 29].

Similar to the two-phase $\mathcal{C}_L$ coefficient for straight pipes, the dimensional analysis in Appendix C proves that the scaled pressure drop of an incompressible isothermal water-air flow across a mitre elbow,

$$\mathcal{K}_L = \frac{\Delta p^*|_e D^{*4} \rho_L^*}{\dot{m}_L^2}, \tag{10}$$

can be expressed as $\mathcal{K}_L = \mathcal{K}_L\left(\mathcal{R}e_L, \mathcal{R}e_G, Fr_L\right)$. Figs. 23 and 24 show the scaled drop of pressure $\mathcal{K}_L$ for the horizontal and the horizontal to vertical upward configurations, respectively. Differently from the frictional pressure drop in the straight portions of the pipe, the pressure drop across the sharp bend is significantly affected by the flow patterns. The highest data scatter in Figs. 23 and 24 is observed for slug and slug-annular flows, whereas the data for annular and plug flows instead collapse well, i.e., in the cases of large inertia due to large air flow rates, i.e., large $\mathcal{R}e_G$, and to large inertia due to large water flow rates, i.e., large $\mathcal{R}e_L$. The effect of Fr_L $(0.5 \leq Fr_L \leq 2.5)$ on the pressure drop across the elbows is mild. The high scatter for intermittent flows is not due to the effect of the Froude number as in the vertical case but to the separation and secondary flows in elbows, which are more influential than gravity in this case.

New pattern-based correlations are proposed to fit the scaled pressure drop across the mitre elbows. For the horizontal case the following correlation is proposed for intermittent (plug and slug) flows:

$$\mathcal{K}_L \mathcal{R}e_G^{0.3} = 127.3\left(\frac{\mathcal{R}e_L}{\mathcal{R}e_G}\right)^{-0.89} + 1.472, \qquad \left(\frac{\mathcal{R}e_L}{\mathcal{R}e_G}\right)^{0.5} > 1. \tag{11}$$

For slug-annular and annular flows in the horizontal case, we propose the following correlation:

$$\mathcal{K}_L \mathcal{R}e_G^{0.3} = 40.25\left(\frac{\mathcal{R}e_L}{\mathcal{R}e_G}\right)^{-1.75} + 102.1, \qquad \left(\frac{\mathcal{R}e_L}{\mathcal{R}e_G}\right)^{0.5} < 1. \tag{12}$$

Correlation (11) fits 83% of the data with $\mathcal{E} = 23.6\%$, while correlation (12) fits 90% of the data with $\mathcal{E} = 14.2\%$. Correlation (12) also fits the annular flow data only with the same accuracy.

For the horizontal to vertical upward configuration the following correlation is proposed for intermittent (plug and slug) flows:

$$\mathcal{K}_L \mathcal{R}e_G = 41370\left(\frac{\mathcal{R}e_L}{\mathcal{R}e_G}\right)^{-1.03} - 321.2, \qquad \left(\frac{\mathcal{R}e_L}{\mathcal{R}e_G}\right)^{0.5} > 1. \tag{13}$$

For slug-annular and annular flows in the horizontal to vertical upward configuration, the following correlation is proposed:

$$\mathcal{K}_L \mathcal{R}e_G = 25570\left(\frac{\mathcal{R}e_L}{\mathcal{R}e_G}\right)^{-2.31} + 16790, \qquad \left(\frac{\mathcal{R}e_L}{\mathcal{R}e_G}\right)^{0.5} < 1. \tag{14}$$

Correlations (13) and (14) predict the scaled experimental data with $\mathcal{E} = 28.6\%$ and $\mathcal{E} = 23.9\%$, respectively. Slug-flow data, occurring for $1 < (\mathcal{R}e_L/\mathcal{R}e_G)^{0.5} < 3$, are too scattered and could not be correlated.
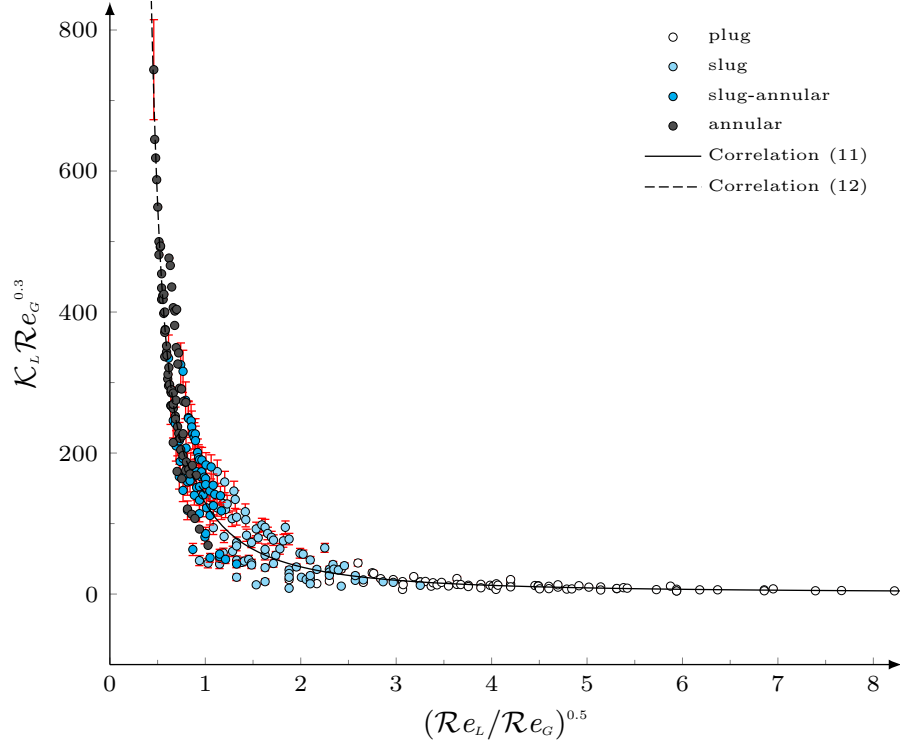
Figure 23: Scaled two-phase pressure drop across the horizontal mitre elbows.
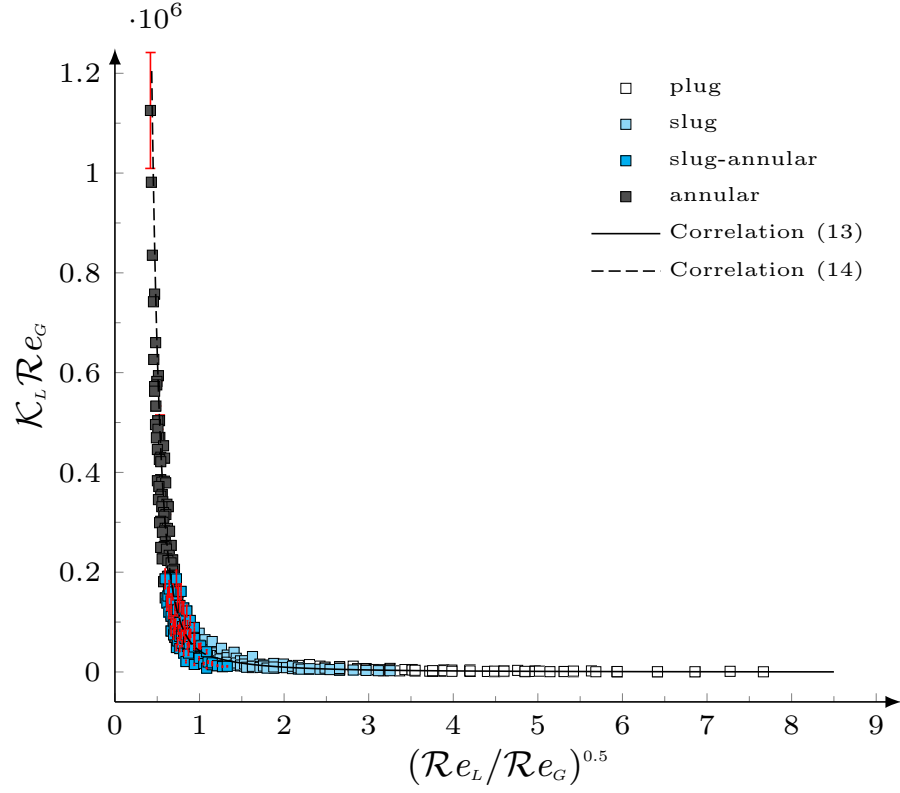

Figure 24: Scaled two-phase pressure drop across the horizontal to vertical mitre elbows.

4. Conclusions

Water-air flow has been studied experimentally in horizontal and vertical straight pipes and across $90°$ sharp-angled mitre elbows. The portion of the pipe upstream of the elbow was always positioned horizontally, while the portion of the pipe downstream of the bend was oriented horizontally or vertically with the flow moving upward. The flow patterns have been investigated visually and the pressure drops along the straight pipes and across the mitre elbows have been measured.

The observed flow patterns in the straight pipes have been predicted well by the Mandhane map [13] for the horizontal orientation and by the Hewitt-Roberts map [14] for the vertical orientation. A dimensional analysis has allowed us to express these maps in scaled form, i.e., as a function of the Reynolds numbers $\mathcal{R}e_L$ and $\mathcal{R}e_G$ based on the superficial velocities of water and air respectively, thereby obtaining a slightly improved agreement between our data and the prediction given by the maps. The analysis further reveals the mild influence of the Froude number for the range of flow parameters investigated. Future work should be directed to obtain non-dimensional water-air pattern maps in the $(\mathcal{R}e_L, \mathcal{R}e_G)$ space at fixed Froude number.

As the fluids pass through the mitre elbows, the changes of flow patterns occur at Reynolds numbers that are lower than in round elbows because the centrifugal and secondary-flow effects are more intense when the elbow is sharp. For the first time, we have observed slug flow with multiple membranes in the vertical upward condition as a result of bubbles merging downstream of the bend. The membrane flow has been detected in ranges of j_L^* that are larger than those reported by Milan *et al.* [20] for downward flow. We have proposed a new representation for the changes of the flow patterns occurring as the fluids pass through the sharp elbows. We have used a rescaled Mandhane map for each orientation where the position of the data point in the flow region represents the flow regime upstream of the elbow and the colour of the symbol indicates the new pattern that emerges as the fluids pass through the elbow.

We have also obtained new pattern-based correlations to fit the scaled experimental data for the flows through the straight pipes and across the elbows. These correlations are more accurate than the models presently available in the literature.

References

[1] C. Brennen, Fundamentals of multiphase flow, Cambridge University Press, 2005.

[2] R. Lockhart, R. Martinelli, Proposed correlation of data for isothermal two-phase, two-component flow in pipes, Chem. Eng. Prog. 45 (1) (1949) 39–48.

[3] D. Chisholm, Pressure gradients due to friction during the flow of evaporating two-phase mixtures in smooth tubes and channels, Int. J. Heat Mass Trans. 16 (2) (1973) 347 – 358.

[4] A. Dukler, M. Wicks, R. Cleveland, Frictional pressure drop in two-phase flow: B. an approach through similarity analysis, AIChE J. 10 (1) (1964) 44–51.

[5] L. Friedel, Improved friction pressure drop correlations for horizontal and vertical two-phase pipe flow, in: European two-phase flow group meeting, Paper E, Vol. 2, 1979, p. 1979.

[6] H. Müller-Steinhagen, K. Heck, A simple friction pressure drop correlation for two-phase flow in pipes, Chem. Eng. and Proc.: Process Intensification 20 (6) (1986) 297–308.

[7] D. Chisholm, Two-phase flow in bends, Int. J. Multiph. Flow 6 (4) (1980) 363–367.

[8] A. Azzi, L. Friedel, Two-phase upward flow 90 bend pressure loss model, Forschung im Ingenieurwesen 69 (2) (2005) 120–130.

[9] F. Sánchez Silva, J. Luna Resendiz, I. Carvajal Mariscal, R. Tolentino Eslava, Pressure drop models evaluation for two-phase flow in 90 degree horizontal elbows, Ingeniería mecánica, tecnología y desarrollo 3 (4) (2010) 115–122.

[10] P. Sookprasong, J. Brill, Z. Schmidt, Two-phase flow in piping components, J. Energy Res. Tech. 108 (3) (1986) 197–201.

[11] C. Wang, C. Youn, H. Shyu, Frictional performance of R-22 and R-410a inside a 5.0 mm wavy diameter tube, Int. J. Heat Mass Trans. 46 (4) (2003) 755–760.

[12] R. Lima, J. Thome, Two–phase pressure drops in adiabatic horizontal circular smooth u-bends and contiguous straight pipes (rp-1444), Hvac&R Research 16 (3) (2010) 383–397.

[13] J. Mandhane, G. Gregory, K. Aziz, A flow pattern map for gas-liquid flow in horizontal pipes, Int. J. Multiph. Flow 1 (4) (1974) 537–553.

[14] G. Hewitt, D. Roberts, Studies of two-phase flow patterns by simultaneous 292 X-ray and flash photography, Tech. rep., Atomic Energy Research Establishment, Harwell (England) (1969).

[15] A. Ghajar, C. C. Tang, Advances in void fraction, flow pattern maps and non-boiling heat transfer two-phase flow in pipes with various inclinations, Adv. Multiphase Flow Heat Trans. 1 (2009) 1–52.

[16] I. Chen, Chi-Chung, Y. Yang, Influence of horizontal return bend on the two-phase flow pattern in a 6.9 mm diameter tube, The Canadian J. Chemical Eng. 80 (3) (2002) 478–484.

[17] C. Wang, Y. C.I., Y. Yang, R. Hu, Influence of horizontal return bend on the two-phase flow pattern in small diameter tubes, Exp. Therm. Fluid Sc. 28 (2) (2004) 145–152.

[18] C.-C. Wang, Y. Chen, Y.-T. Lin, Y.-J. Chang, A visual observation of the air–water two-phase flow in small diameter tubes subject to the influence of vertical return bends, Chem. Eng. Res. Des. 86 (11) (2008) 1223–1235.

[19] L.-C. Hsu, Y. Chen, C.-M. Chyu, C.-C. Wang, Two-phase pressure drops and flow pattern observations in 90° bends subject to upward, downward and horizontal arrangements, Exp. Therm. Fluid Sci. 68 (2015) 484–492.

[20] M. Milan, N. Borhani, J. Thome, A new type of flow structure in cocurrent adiabatic vertically downward air–water flow: Membrane flow, Int. J. Multiph. Flow 58 (2014) 246–256.

[21] K. De Kerpel, B. Ameel, H. Huisseune, C. Ta Joen, H. Canière, M. De Paepe, Two-phase flow behaviour and pressure drop of r134a in a smooth hairpin, Int. J. Heat Mass Trans. 55 (4) (2012) 1179–1188.

[22] M. Padilla, R. Revellin, J. Wallet, J. Bonjour, Flow regime visualization and pressure drops of hfo-1234yf, r-134a and r-410a during downward two-phase flow in vertical return bends, Int. J. Heat Fluid Flow 40 (2013) 116–134.

[23] P. De Oliveira, J. Barbosa, Pressure drop and gas holdup in air–water flow in 180 return bends, Int. J. Multiph. Flow 61 (2014) 83–93.

[24] P. Modi, S. Jayanti, Pressure losses and flow maldistribution in ducts with sharp bends, Chem. Eng. Res. Des. 82 (3) (2004) 321–331.

[25] S. Kim, J. Park, G. Kojasoy, J. Kelly, S. Marshall, Geometric effects of 90-degree elbow in the development of interfacial structures in horizontal bubbly flow, Nuclear Eng. Design 237 (20) (2007) 2105–2113.

[26] M. Yadav, S. Kim, K. Tien, S. Bajorek, Experiments on geometric effects of 90-degree vertical-upward elbow in air water two-phase flow, Int. J. Multiph. Flow 65 (2014) 98–107.

[27] M. Yadav, S. Kim, Effects of 90° vertical elbows on the distribution of local two-phase flow parameters, Nuclear Tech. 181 (1) (2013) 94–105.

[28] S. Z. Rouhani, M. S. Sohal, Two–phase flow patterns: A review of research results, Prog. in Nuc. Ener. 11 (3) (1983) 219–259.

[29] L. Cheng, G. Ribatski, J. Thome, Two-phase flow patterns and flow-pattern maps: fundamentals and applications, Applied Mech. Rev. 61 (5) (2008) 050802.

[30] B. Schmandt, H. Herwig, A standard method to determine loss coefficients of conduit components based on the second law of thermodynamics, in: ASME Conf. Proc., Vol. 73249, 2012.

[31] B. Schmandt, H. Herwig, Loss coefficients for periodically unsteady flows in conduit components: illustrated for laminar flow in a circular duct and a 90 degree bend, ASME J. Fluids Eng. 135 (3) (2013) 031204.

[32] B. Schmandt, H. Herwig, Losses due to conduit components: an optimization strategy and its application, ASME J. Fluids Eng. 138 (3) (2016) 031204.

[33] H. Kirchbach, Loss of energy in miter bends, Trans. Munich. Hydraulic Institute, American Soc. Mech. Eng. 3.

[34] W. Schubart, Energy loss in smooth-and rough-surfaced bends and curves in pipe lines, Trans. Hydraul. Inst. Munich Tech. Univ. 3 (1935) 81–99.

[35] W. Al-Tameemi, P. Ricco, Pressure-loss coefficient of 90 deg sharp-angled miter elbows, ASME J. Fluids Eng. 140 (6) (2018) 061102.

[36] R. Neilson, J. Wood, R. Hamilton, H. Li, A comparison of plastic collapse and limit loads for single mitred pipe bends under in-plane bending, Int. J. of Pressure Vessels and Piping 87 (10) (2010) 550–558.

[37] W. Al-Tameemi, P. Ricco, Pattern–based pressure drop of air–water flow across a 90° sharp mitre elbow, Int. J. Comp. Meth. Exp. Meas. 6 (1) (2018) 198–207.

[38] Y. Xia, M. Alshehhi, Y. Hardalupas, L. Khezzar, Spray characteristics of free air-on-water impinging jets, Int. J. Multiph. Flow 100 (2018) 86–103.

[39] A. Peddu, S. Chakraborty, P. K. Das, Visualization and flow regime identification of downward air–water flow through a 12 mm diameter vertical tube using image analysis, Int. J. Multiph. Flow 100 (2018) 1–15.

[40] R. Verschoof, D. Bakhuis, P. Bullee, S. Huisman, C. Sun, D. Lohse, Air cavities at the inner cylinder of turbulent Taylor–Couette flow, Int. J. Multiph. Flow 105 (2018) 264–273.

[41] E. Lemmon, M. Huber, M. McLinden, NIST Standard Reference Database 23: Reference Fluid Thermodynamic and Transport Properties - REFPROP. 9.0. (2010).

[42] J. Taylor, An Introduction to Error Analysis, University Science Books, 1997.

[43] P. Spedding, V. Nguyen, Regime maps for air water two phase flow, Chem. Eng. Sc. 35 (4) (1980) 779–793.

[44] M. Wang, F. Mayinger, Post-dryout dispersed flow in circular bends, Int. J. Multiph. Flow 21 (3) (1995) 437–454.

[45] P. Spedding, E. Bénard, Gas-liquid two phase flow through a vertical 90 elbow bend, Exp. Therm. Fluid Sc. 31 (7) (2007) 761–769.

[46] S. Kim, G. Kojasoy, T. Guo, Two-phase minor loss in horizontal bubbly flow with elbows: 45-degree and 90-degree elbows, Nuclear Eng. Design 240 (2) (2008) 284–289.

[47] C. Tang, S. Tiwari, A. J. Ghajar, Effect of void fraction on pressure drop in upward vertical two-phase gas-liquid pipe flow, J. Eng. Gas Turb. Power 135 (2) (2013) 022901.

[48] P. Spedding, G. Woods, R. Raghunathan, W. J.K., Vertical two-phase flow: Part iii: Pressure drop, Chem. Eng. Res. Des. 76 (5) (1998) 628–634.

[49] P. Spedding, G. Woods, R. Raghunathan, J. Watterson, Flow pattern, holdup and pressure drop in vertical and near vertical two-and three-phase upflow, Chem. Eng. Res. Des. 78 (3) (2000) 404–418.

[50] H. Liu, C. Vandu, R. Krishna, Hydrodynamics of Taylor flow in vertical capillaries: flow regimes, bubble rise velocity, liquid slug length, and pressure drop, Ind. Eng. Chem. Res. 44 (14) (2005) 4884–4897.

[51] L. Liu, The phenomenon of negative frictional pressure drop in vertical two-phase flow, Int. J. Heat Fluid Flow 45 (2014) 72–80.

[52] X. Statgraphics Centurion, Version 16.1. 17, Statpoint Technologies, Inc.

[53] P. Griffith, C. Lau, P. C. Hon, J. Pearson, Two phase pressure drop in inclined and vertical pipes, Tech. rep., Cambridge: Heat Transf. Lab., 1973 (1973).

[54] A. Dasgupta, D. Chandraker, S. Kshirasagar, B. Reddy, R. Rajalakshmi, A. Nayak, S. Walker, P. Vijayan, G. Hewitt, Experimental investigation on dominant waves in upward air-water two-phase flow in churn and annular regime, Exp. Therm. Fluid Sc. 81 (2017) 147–163.

[55] L. S. Tong, Boiling heat transfer and two-phase flow, Routledge, 2018.

[56] Z. Yang, M. Gong, G. Chen, X. Zou, J. Shen, Two-phase flow patterns, heat transfer and pressure drop characteristics of r600a during flow boiling inside a horizontal tube, Applied Therm. Eng. 120 (2017) 654–671.

[57] Y. Chen, C.-C. Wang, S. Lin, Measurements and correlations of frictional single-phase and two-phase pressure drops of r-410a flow in small u-type return bends, Int. J. Heat Mass Trans. 47 (10) (2004) 2241–2249.

[58] I. Chen, Y.-S. Wu, J.-S. Liaw, C.-C. Wang, Two-phase frictional pressure drop measurements in u-type wavy tubes subject to horizontal and vertical arrangements, Appl. Therm. Eng. 28 (8) (2008) 847–855.

[59] A. Sur, D. Liu, Adiabatic air–water two-phase flow in circular microchannels, Int. J. Therm. Sc. 53 (2012) 18–34.

Appendix A. Computation of the frictional pressure drop along the straight portions of the pipe

The frictional pressure drop per unit length along the straight portions of the pipe is computed as follows [51, 53]:

$$\frac{\Delta p^*}{\Delta l^*}\bigg|_{\mathrm{f}} = \frac{\Delta p^*}{\Delta l^*}\bigg|_{\mathrm{meas}} - \frac{\Delta p^*}{\Delta l^*}\bigg|_{\mathrm{st}}\sin\theta, \tag{A.1}$$

where the angle θ is measured with respect the vertical line, the subscript "meas" denotes the total measured pressure drop per unit length and the subscript "st" indicates the static pressure drop per unit length due to the effect of gravity and defined as:

$$\frac{\Delta p^*}{\Delta l^*}\bigg|_{\mathrm{st}} = g^*\left[(1-\epsilon)\rho_L^* + \epsilon\rho_G^*\right], \tag{A.2}$$

where ϵ is the gas-phase void fraction, ρ_L^* is the density of water, and ρ_G^* is the density of air. The image processing technique was used to evaluate the gas-phase void fraction [54, 55, 56]. Twenty different snapshots were captured from each video at all the flow conditions listed in Table 2. The captured photos at each flow condition were converted to binary images, as shown in Fig.A.25 for the slug and annular flows. The binary images were then analyzed by using IMAGEJ software to compute the values of the void fraction. The void fraction values were evaluated from the captured images at each flow rate and averaged to compute the void fraction value at that flow rate.
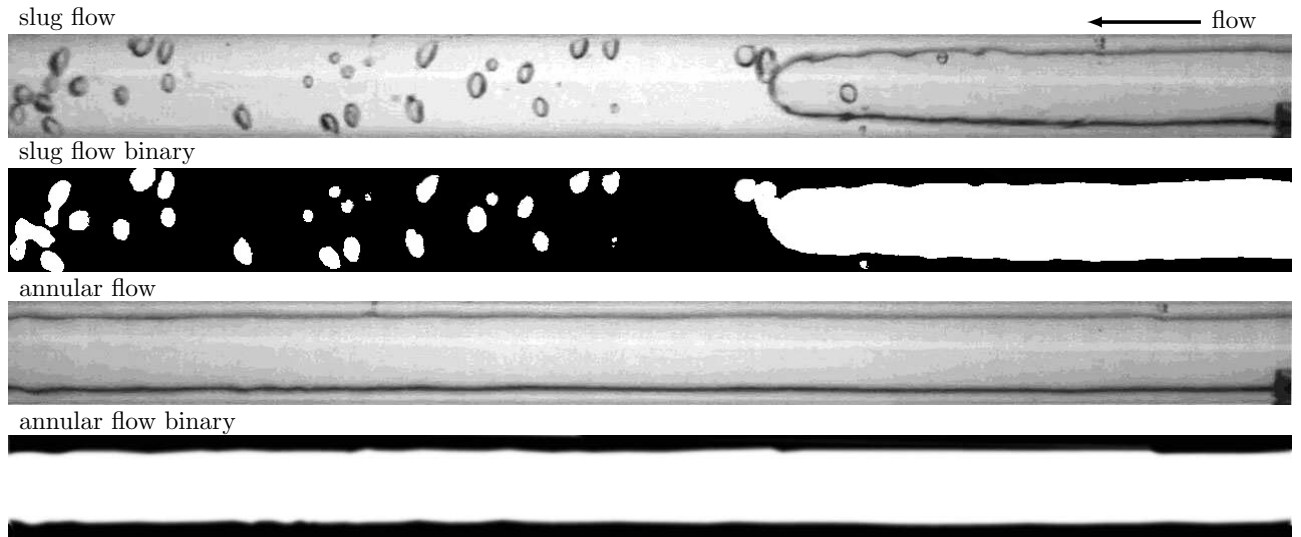

Figure A.25: Comparison between the captured photos from the flow videos and the converted images to a binary form, for D^*=11mm.

In Fig. A.26, the computed frictional pressure drops in straight pipes for horizontal and vertical orientations are compared with the predictions of three widely-used models.
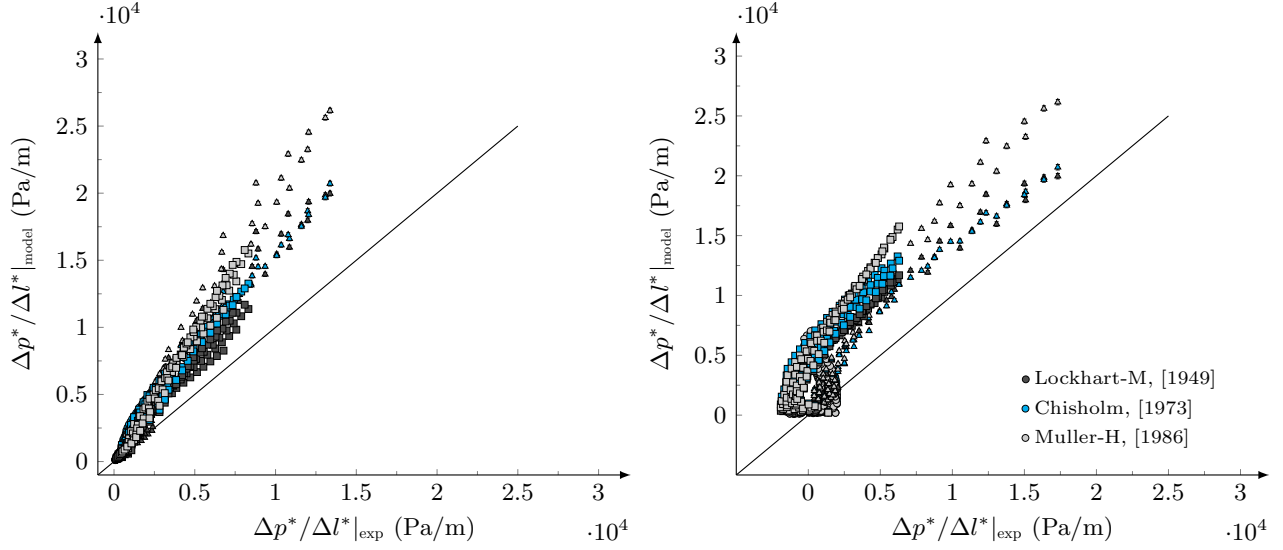
Figure A.26: Comparison between the experimental pressure drop along horizontal straight pipes (left) and vertical straight pipes (right), with Lockhart and Martinelli [2], Chisholm [3] and Muller and Heck [6] models, for D^*=11mm ($\triangle$), D^*=16mm ($\square$), and D^*=21mm ($\circ$).
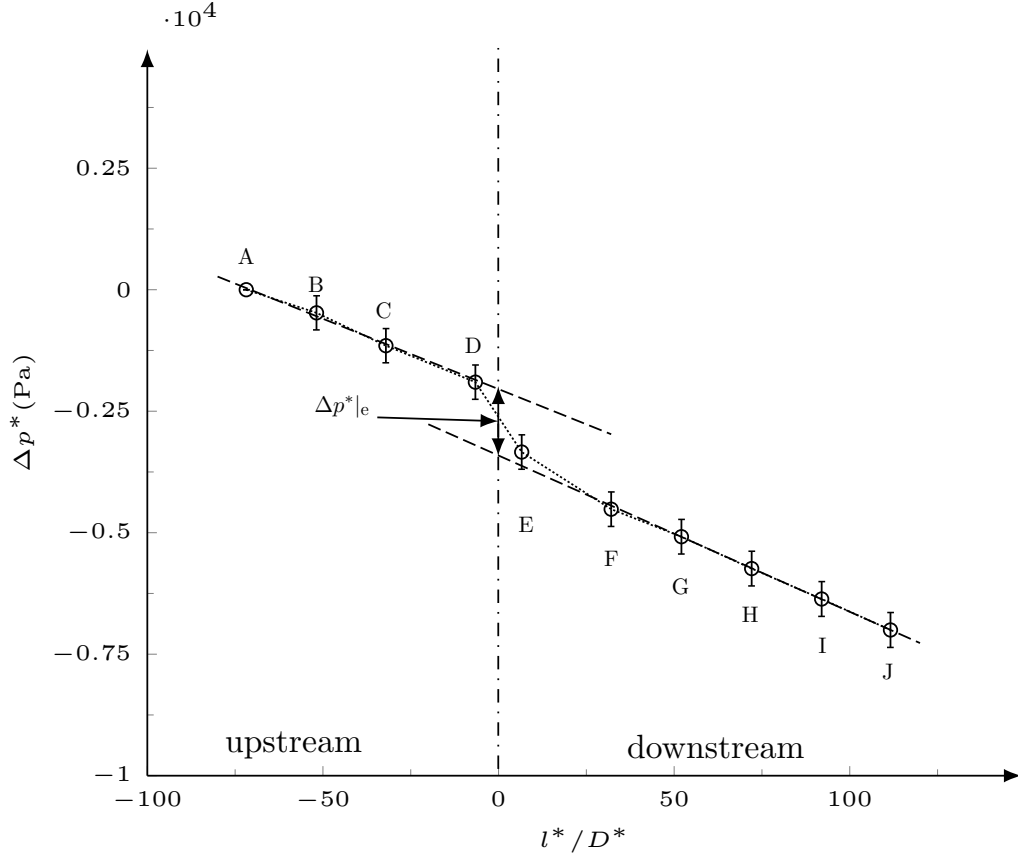

Figure B.27: Water-air pressure drop relative to the measurement location A along the 21-mm-diameter test section for $\mathcal{R}e_L$=9330 and $\mathcal{R}e_G$=8466 in the horizontal configuration.

Appendix B. Computation of the pressure drop across the mitre elbow

Fig. B.27 represents the two-phase pressure drop along the pipe with D^*=21mm and across the mitre elbow in the horizontal configuration as a function of the scaled distance l^*/D^* from the elbow. The effect of the elbow is negligible at a distance of $32.5D^*$ upstream of the elbow (measurement location C) and at a distance of $60D^*$ downstream of the sharp bend (measurement location G), where the gradient of the pressure is only
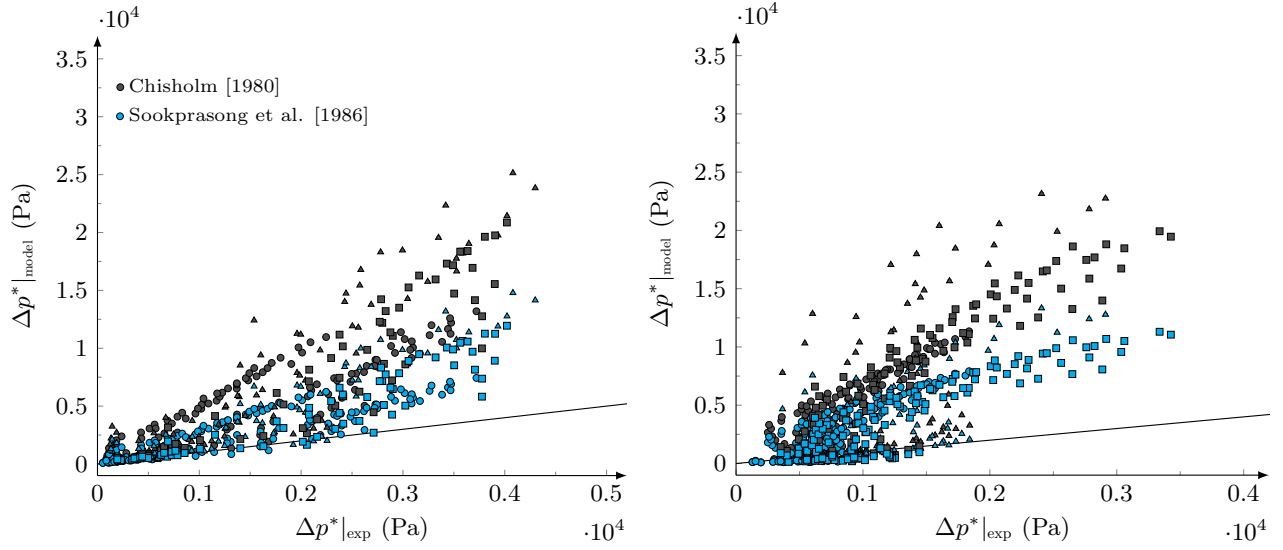
26

Figure B.28: Comparison between the experimental pressure drop across the horizontal (left) and vertical (right) 90° sharp-angled mitre elbows with Chisholm [7] and Sookprasong [10] models, for D^*=11mm ($\triangle$), D^*=16mm ($\square$), and D^*=21mm ($\circ$).

caused by the distributed straight-pipe friction.

As shown in Fig. B.27, the drop of pressure across the sharp bend, $\Delta p^*|_e$, is computed as the difference between the two best-fit straight lines defining the straight-pipe pressure gradients upstream and downstream of locations C and G, represented by the dashed lines, at l^*/D^*=0, denoted by the vertical dashdotted line. The pressure drop across the horizontal and horizontal to vertical sharp bends are compared with the Chisholm [7] and Sookprasong [10] models, as shown in Fig. B.28.

Appendix C. Dimensional analysis

A dimensional analysis based on the Π theorem is employed to obtain the non-dimensional parameters that describe the water-air flow. The flow-pattern maps, the friction coefficient $\mathcal{C}_L$, and the scaled pressure drop of the elbow $\mathcal{K}_L$ are expressed as functions of these parameters. The flow depends on the diameter D^*, the densities of the fluids ρ_k^*, the dynamic viscosities of the fluids μ_k^*, the mass flow rates $\dot{m}_k^*$ (where $k = L$ for water and $k = G$ for air), and the gravitational acceleration g^*. The flow is also dependent on the angle of the pipe inclination with respect to the vertical axis. For mitre elbows, the flow also depends on the flow direction, as explained in §3.1.2. As we consider flows at high Reynolds numbers, at high Weber numbers in the range $We = \rho_L^* j_L^{*2} D^*/\sigma^* =$25.3-159.7 (where σ^* is the surface tension of water), and through pipes with diameters larger than 3mm, the effect of the surface tension between air and water is negligible [57, 58, 59].

The number of dimensionless parameters is $\Pi = k' - n$, where $k' = 8$ is the number of the dimensional parameters and $n = 3$ is the number of basic dimensions, i.e., the mass, the length, and the time. It follows that $\Pi = 5$. As repeating variables, we choose D^*, ρ_L^*, and $\dot{m}_L^*$. We find the following dimensionless parameters:

$$\Pi_1 = \mathcal{R}e_L = \frac{\dot{m}_L^*}{\mu_L^* D^*} = \frac{\rho_L^* j_L^* D^* \pi}{4\mu_L^*}.$$

$$\Pi_2 = \mathcal{R}e_G = \frac{\dot{m}_G^*}{\mu_G^* D^*} = \frac{\rho_G^* j_G^* D^* \pi}{4\mu_G^*}.$$

$$\Pi_3 = Fr_L = \frac{\dot{m}_L^*}{\sqrt{g^* D^{*5/2} \rho_L^*}}.$$

$$\Pi_4 = R = \frac{\rho_L^*}{\rho_G^*}.$$

$$\Pi_5 = \mathcal{V} = \frac{\mu_L^*}{\mu_G^*}.$$

The Π_5 parameter found directly from the analysis is $\Pi_5 = \dot{m}_G^*/\dot{m}_L^*$, which can be written as $\Pi_5 = (\mu_L^*/\mu_G^*)\,\mathcal{R}e_L/\mathcal{R}e_G$. The Reynolds numbers already belong to the dimensionless group of parameters and therefore the ratio of viscosities $\mathcal{V}$ is a more convenient choice for Π_5. For a specified geometry and flow direction, the flow patterns

can therefore be expressed in terms of $\mathcal{R}e_L$, $\mathcal{R}e_G$, Fr_L, R, and $\mathcal{V}$. For an incompressible and isothermal water-air flow, R and $\mathcal{V}$ are constants, and thus the flow pattern maps can be shown in the two-dimensional space $(\mathcal{R}e_L,\ \mathcal{R}e_G)$ for a given Fr_L. In order to minimize the possible changes of air density due to acceleration we have utilized a mass flow meter to measure the air flow rates. The maximum change in the air density was 0.05kg/m^3, i.e., about 3%, computed by using the NIST Refprop software [41]. Therefore, the density ratio R could be considered constant.

The pressure-drop coefficients $\mathcal{C}_L = (\Delta p^*/\Delta l^*|_{\mathrm{f}})\, D^{*5}\rho_L^*/\dot{m}_L^2$ and $\mathcal{K}_L = \Delta p^*|_{\mathrm{e}} D^{*4}\rho_L^*/\dot{m}_L^2$ can therefore be expressed as

$$\mathcal{C}_L = \mathcal{C}_L\left(\mathcal{R}e_L,\ \mathcal{R}e_G,\ Fr_L\right), \tag{C.1}$$

and

$$\mathcal{K}_L = \mathcal{K}_L\left(\mathcal{R}e_L,\ \mathcal{R}e_G,\ Fr_L\right) \tag{C.2}$$

because R and $\mathcal{V}$ are assumed constant. Note that the subscript L for $\mathcal{C}_L$ and $\mathcal{K}_L$ denotes the adopted scaling through ρ_L^* and $\dot{m}_L$ of water, although these are two-phase quantities.